This article has been accepted for publication in a future issue of this journal, but has not been fully edited. Content may change prior to final publication. Citation information: DOI 10.1109/TIA.2018.2829459, IEEE Transactions on Industry Applications

Generalized Multi-Frequency Current Controller for Grid-Connected Converters With LCL Filter

Diego Pérez-Estévez, *Student Member, IEEE*, Jesús Doval-Gandoy, *Member, IEEE*,
Alejandro G. Yepes, *Member, IEEE*, Óscar López, *Senior Member, IEEE*,
and Fernando Baneira, *Student Member, IEEE*,
Applied Power Electronics Technology Research Group, EII, University of Vigo, Vigo, Spain
E-mail: {dieperez,jdoval,agyepes,olopez,fbaneira}@uvigo.es

***Abstract*—This article presents a grid-side current controller for grid-tied inverters with LCL filter, including harmonic current elimination. The proposed controller only measures the grid current and voltage and it combines excellent dynamic characteristics with good robustness. Contrarily to previously proposed harmonic-current controllers, the presented solution offers a generalized method that gives a consistent (with minimal variation in the reference-tracking dynamics) and stable performance irrespectively of the number of current harmonics to be canceled and of the resonant frequency of the LCL filter (provided that it is lower than the Nyquist frequency). The response to reference commands is completely damped and fast. The response speed is set in accordance with the low-pass characteristic of the LCL filter so as to limit the control effort. Concerning the disturbance rejection, the controller offers an infinite impedance to any disturbances (such as grid voltage harmonics) at a set of arbitrarily specified frequencies. This allows the designer to eliminate all the undesired current harmonics with a simple design process. In addition, the performance of the presented controller is evaluated in terms of a fundamental tradeoff that exists between robustness to variations in the grid impedance and the number of frequency components rejected. Finally, simulation and experimental results that validate the proposal are presented.**

***Index Terms*—Current harmonics, grid-connected converter, LCL filter, state-space current control.**

I. Introduction

Distributed power generation systems (DPGSs) and microgrids are gaining popularity due to the increasing use of renewable energy sources [1]. In this context, the voltage source converter (VSC) plays a crucial role in the effective integration of the different elements that conform a microgrid. The electronic power conditioning and control of the energy production are central aspects that should be addressed for a successful integration of DPGSs. However, the large penetration of these systems demands more stringent interconnection requirements [2]. In order to meet these requisites under different grid conditions [3], a current controller with harmonic control becomes necessary to eliminate harmonics caused by grid voltage harmonics and VSC nonlinearities.

Current harmonics produce increased losses, operational problems, and equipment deterioration [2]. LCL filters are commonly used in place of traditional L filters because they attenuate current harmonics generated by the switching voltage of the VSC with a slope of 60 dB per decade [4]. This high attenuation allows the designer to reduce the reactive elements while maintaining a low switching ripple in the grid-side current. Nonetheless, this improved performance of the LCL filter also augments the complexity of the system to be controlled due to the appearance of a high-quality-factor resonant circuit [4].

Different controllers for grid-tied VSCs with LCL filter capable of eliminating low-order harmonics in the grid-side current have been proposed [5]–[20]. Some of the proposed solutions use techniques from modern control theory [5], [20] or sophisticated feedforward schemes [6], [7]; however, conventional proportional-integral (PI) [8]–[11] and proportional-resonant (PR) [12]–[19] controllers placed in different frames (so as to selectively target the desired harmonics) are the most commonly adopted solutions in the literature.

A common problem of these solutions [5]–[18], [20]–[22] is the existence of a tradeoff between the reference-tracking and the disturbance-rejection capability during transients [16]: if the reference tracking is improved by a change in the controller gains, then the disturbance rejection worsens (and viceversa). In addition, the transient response (to both disturbance and reference changes) is degraded as the number of controlled harmonics (or the number of paralleled regulators) increases, because of the additional poles in the system [16].

Another common problem of these harmonic-current controllers is the reduced stability margin when an LCL filter is used [13], due to the aforementioned resonance. In [23]–[25], such problem has been studied for the case of a single-frequency controller using PI or PR controllers. The solution presented in [23] can provide a stable system for a wide range of resonant frequencies of the LCL filter measuring only the grid-side current. The method proposed in [24] introduces a

Manuscript received xxxxx; revised xxxxx; accepted xxxxx. Date of current version xxxxx. Paper xxxxxx, presented at the 2017 IEEE Energy Conversion Congress and Exposition, Cincinnati, OH, USA, Oct. 1-5, and approved for publication in the IEEE TRANSACTIONS ON INDUSTRY APPLICATIONS by the Industrial Power Converter Committee of the IEEE Industry Applications Society. This work was supported by the Spanish Ministry of Science and Innovation and by the European Commission, European Regional Development Fund (ERDF) under project DPI2016-75832 and the FPU scholarship FPU14/00683.

All the authors are with the Applied Power Electronics Technology Group (APET), University of Vigo, Vigo 36310, Spain (e-mail: dieperez@uvigo.es; jdoval@uvigo.es; agyepes@uvigo.es; olopez@uvigo.es; fbaneira@uvigo.es).

Color versions of one or more of the figures in this paper are available online at http://ieeexplore.ieee.org.

Digital Object Identifier xxxxx

This article has been accepted for publication in a future issue of this journal, but has not been fully edited. Content may change prior to final publication. Citation information: DOI 10.1109/TIA.2018.2829459, IEEE Transactions on Industry Applications

time delay to achieve stability when the grid-side current is fed back. In [25], an active damping technique for the resonance of the LCL is presented. However, such results cannot be directly applied to a system with a multi-frequency controller because adding more integral or resonant parts to the system changes its robustness. To the authors' knowledge, a transfer-function-based controller that meets a multi-frequency control requirement and can provide a stable operation for a wide range of resonant-to-sampling-frequency ratios using only the grid-side current measurements has not been published yet. Consequently, additional damping mechanisms [6], [7], [13], [17]–[19] are often needed to achieve stability under certain ratios of sampling-to-resonant frequency [26]. Finally, direct pole-placement schemes such as [20]–[22] give good robustness and good dynamics with a simple structure, but they do not completely eliminate the grid-induced current harmonics: only the fundamental frequency of the grid voltage is controlled with zero steady-state error.

This article is an extension of the conference version [27] and proposes a current controller for grid-tied inverters that offers an infinite impedance to voltage disturbances at an arbitrarily specified set of frequencies. This work has the following advantages compared to previous multi-frequency proposals:

- A stable operation, irrespectively of the resonant frequency of the LCL filter f_{res}, provided that it is lower than the Nyquist frequency of the digital controller $f_{\mathrm{s}}/2$. In particular, the presented method has been experimentally verified when f_{res} is equal to the critical resonant frequency where a conventional controller cannot stabilize the system ($f_{\mathrm{res}} = f_{\mathrm{s}}/6$) [26].
- A better robustness to variations in the grid impedance compared to recently published PR- or PI-based controllers due to the absence of a critical resonant frequency where the system becomes unstable. An analysis of the robustness depending on the number of current harmonics controlled with zero steady-state error is also included.
- An improved reference-tracking performance without affecting the disturbance-rejection capabilities. The response to reference commands is equivalent to that of a first-order system (without overshoot, nor axis cross-coupling) and the speed can be set at the design stage in accordance with the low-pass characteristic of the LCL filter so as to limit the controller effort and avoid overmodulation.

As regards the computational load, the controller proposed in this paper requires a higher computational load, as given in Appendix B, in comparison to transfer-function-based methods. Nonetheless, modern microcontrollers can successfully execute the required operations without problems even when a large number of frequencies are controlled with zero steady-state error.

After this introduction, Section II presents the model of the plant (the VSC and the LCL filter) and the disturbances. Next, in Section III such model is used to design the observer included in the controller. Section IV demonstrates and justifies the characteristics and performance of the proposed controller.

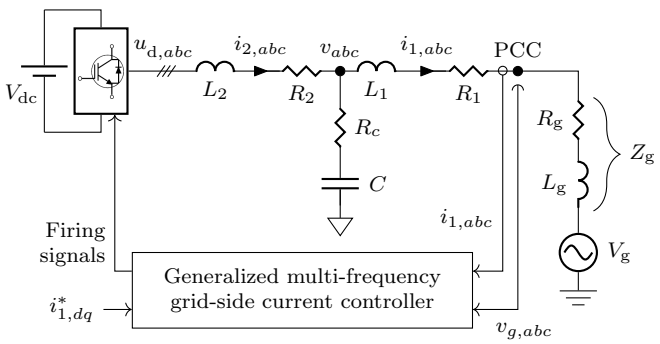

Fig. 1. Grid-tied VSC with LCL filter and grid-side multi-frequency current controller.

Section V assesses the robustness of the proposal to variations in the grid impedance. Section VI presents simulation and experimental results that validate the theory. Conclusions in Section VII close the work.

II. Modeling of the Plant and the Disturbance

This section presents the state-space model of the plant and the disturbance used to design the controller. Fig. 1 depicts the physical plant, which consists of a VSC connected to the grid using an LCL filter. L_1, L_2, and C are the values of the reactive elements of the LCL filter. R_1, R_2, and R_c model the equivalent series resistances of the filter and the VSC [28]. $v_{g,abc}$ is the grid voltage at the point of common coupling (PCC). R_{g} and L_{g} are the values of the resistive and inductive components of the grid impedance Z_{g}. Since these values are usually unknown, they are assumed to be zero to design the controller. $i_{1,abc}$ and $i^*_{1,dq}$ denote the measured grid-side current in the abc frame and the grid-side current reference in the direct quadrature (dq) frame, respectively. If the subscript in a variable does not specify a reference frame, the $\alpha\beta$ frame is assumed.

A block diagram representation of the plant model in the $\alpha\beta$ frame is shown in Fig. 2, where. u_{sat} is the saturated controller output voltage; u_{d} is the pulse width modulator (PWM) voltage reference, e.g., it is the one-sample-delayed saturated controller output voltage; and u'_{d} is the VSC output voltage.

The discrete-time modeling process that describes the LCL filter, the PWM, and the computational delay of this system was presented in [22] and is repeated here for the sake of completeness and continuity. Such modeling process takes place in several steps; each step adds features to the model obtained in the previous stage. In the first place, a continuous model of the LCL filter in stationary frame is presented. This model relates the grid-side current $i_1(t)$ to the VSC output voltage $u'_d(t)$, cf. Fig. 2. The first-order differential equations

This article has been accepted for publication in a future issue of this journal, but has not been fully edited. Content may change prior to final publication. Citation information: DOI 10.1109/TIA.2018.2829459, IEEE Transactions on Industry Applications

in the continuous domain (written in state-space form) are

$$\frac{d\mathbf{x}(t)}{dt} = \underbrace{\begin{bmatrix} \frac{-R_1}{L_1} & 0 & \frac{1}{L_1} \\ 0 & \frac{-R_2}{L_2} & \frac{-1}{L_2} \\ \frac{CR_cR_1-L_1}{CL_1} & \frac{L_2-CR_cR_2}{CL_2} & \frac{-(R_cL_1+R_cL_2)}{L_1L_2} \end{bmatrix}}_{\mathbf{A}} \mathbf{x}(t) + \underbrace{\begin{bmatrix} 0 \\ \frac{1}{L_2} \\ \frac{R_c}{L_2} \end{bmatrix}}_{\mathbf{B}} u'_d(t)$$

$$i_1(t) = \underbrace{\begin{bmatrix} 1 & 0 & 0 \end{bmatrix}}_{\mathbf{C}} \mathbf{x}(t)$$

$$\mathbf{x}(t) = \begin{bmatrix} i_1 & i_2 & v \end{bmatrix}^{\mathrm{T}}. \tag{1}$$

Boldface denotes a vector or a matrix. Equation (1) does not include the effect of the grid voltage v_g in the state variables. This voltage disturbance is handled in a special way, using a disturbance estimation method [29]. .

Next, (1) is discretized by using a zero-order hold (ZOH) equivalent [29]. This discretization method takes into account the half a sample delay added by the PWM [28].

$$\begin{aligned} \mathbf{F} &= e^{\mathbf{A}T_s} \\ \mathbf{G} &= \mathbf{A}^{-1}(e^{\mathbf{A}T_s} - \mathbf{I_4})\mathbf{B} \\ \mathbf{H} &= \mathbf{C}, \end{aligned} \tag{2}$$

where $\mathbf{I_4}$ is the 4×4 identity matrix. The sampling period T_s is equal to a switching period if a single-update strategy is used, and half the switching period in the case of a double-update strategy. The resulting model relates the modulator voltage reference $u_{\mathrm{d}}(k)$ with the sampled grid-side current $i_1(k)$:

$$\begin{aligned} \mathbf{x}(k+1) &= \mathbf{F}\mathbf{x}(k) + \mathbf{G}u_{\mathrm{d}}(k) \\ i_1(k) &= \mathbf{H}\mathbf{x}(k). \end{aligned} \tag{3}$$

Then, a one-sample input (computational) delay is added. The model of this delay on the saturated controller output voltage $u(k)$ is [29]

$$u_{\mathrm{d}}(k+1) = u_{\mathrm{sat}}(k). \tag{4}$$

In this manner, combining (3) and (4), the system model that takes the computational delay into account is

$$\underbrace{\begin{bmatrix} \mathbf{x}(k+1) \\ u_{\mathrm{d}}(k+1) \end{bmatrix}}_{\mathbf{x}_2(k+1)} = \underbrace{\begin{bmatrix} \mathbf{F} & \mathbf{G} \\ \mathbf{0} & 0 \end{bmatrix}}_{\mathbf{F_2}} \underbrace{\begin{bmatrix} \mathbf{x}(k) \\ u_{\mathrm{d}}(k) \end{bmatrix}}_{\mathbf{x}_2(k)} + \underbrace{\begin{bmatrix} \mathbf{0} \\ 1 \end{bmatrix}}_{\mathbf{G_2}} u_{\mathrm{sat}}(k)$$

$$i_1 = \underbrace{\begin{bmatrix} \mathbf{H} & 0 \end{bmatrix}}_{\mathbf{H_2}} \underbrace{\begin{bmatrix} \mathbf{x}(k) \\ u_{\mathrm{d}}(k) \end{bmatrix}}_{\mathbf{x}_2(k)}$$

$$\mathbf{x}_2(k) = \begin{bmatrix} i_1 & i_2 & v & u_{\mathrm{d}} \end{bmatrix}^{\mathrm{T}}. \tag{5}$$

The final model relates the grid-side current $i_1(k)$ to the modulator voltage $u(k)$ in the plant shown in Fig. 2.

In order to obtain zero steady-state error in the grid-side current at a set of desired frequencies, the model of the plant in (5) is augmented with a complex disturbance model that includes the selected frequencies.

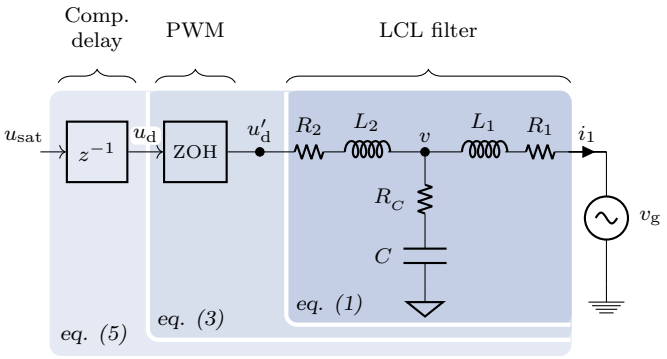

Fig. 2. Stationary-frame plant diagrams: LCL filter, PWM (modeled as a ZOH), and one-sample computational delay.

An h-order harmonic voltage disturbance as a function of time $w_h(t)$ in the $\alpha\beta$ frame has the following expression:

$$w_h(t) = A_h e^{j(\omega_g h t + \phi_h)} \tag{6}$$

where A_h and ϕ_h are the amplitude and initial phase, respectively. The grid fundamental frequency is $\omega_g = 2\pi f_g$. The sign of h defines the sequence (positive or negative) of the harmonic [12]. Zero-sequence voltage harmonics are not included in the disturbance model because they do not produce any current circulation in a three-wire system. A multi-frequency disturbance $w(t)$ that is composed of n harmonics $(h_1, h_2, \ldots, h_n)$ is modeled using (6) as

$$w(t) = w_{h_1}(t) + w_{h_2}(t) + \cdots + w_{h_n}(t). \tag{7}$$

This disturbance equation models all the harmonics (and the fundamental components, for $h = \pm1$) that are to be rejected with zero steady-state error.

The single-frequency disturbance $w_h(t)$ in (6) is a solution of the following differential equation:

$$\frac{dw_h(t)}{dt} = j\omega_g h w_h(t). \tag{8}$$

Hence, the multi-frequency disturbance in (7) can be expressed in matrix notation as a solution of

$$\frac{d\mathbf{r}(t)}{dt} = \underbrace{\begin{bmatrix} j\omega_g h_1 & 0 & \cdots & 0 \\ 0 & j\omega_g h_2 & \cdots & 0 \\ \vdots & \vdots & \ddots & \vdots \\ 0 & 0 & \cdots & j\omega_g h_n \end{bmatrix}}_{\mathbf{A_d}} \mathbf{r}(t)$$

$$w(t) = \underbrace{\begin{bmatrix} 1 & 1 & \cdots & 1 \end{bmatrix}}_{\mathbf{C_d}} \mathbf{r}(t) \tag{9}$$

where

$$\mathbf{r}(t) = \begin{bmatrix} w_{h_1} & w_{h_2} & \cdots & w_{h_n} \end{bmatrix}^{\mathrm{T}}. \tag{10}$$

Then, the model in (9) is discretized by using a ZOH equivalent [29] (to model the PWM effect) [22]:

$$\begin{aligned} \mathbf{F_d} &= e^{\mathbf{A_d}T_s} \\ \mathbf{H_d} &= \mathbf{C_d}. \end{aligned} \tag{11}$$

This article has been accepted for publication in a future issue of this journal, but has not been fully edited. Content may change prior to final publication. Citation information: DOI 10.1109/TIA.2018.2829459, IEEE Transactions on Industry Applications

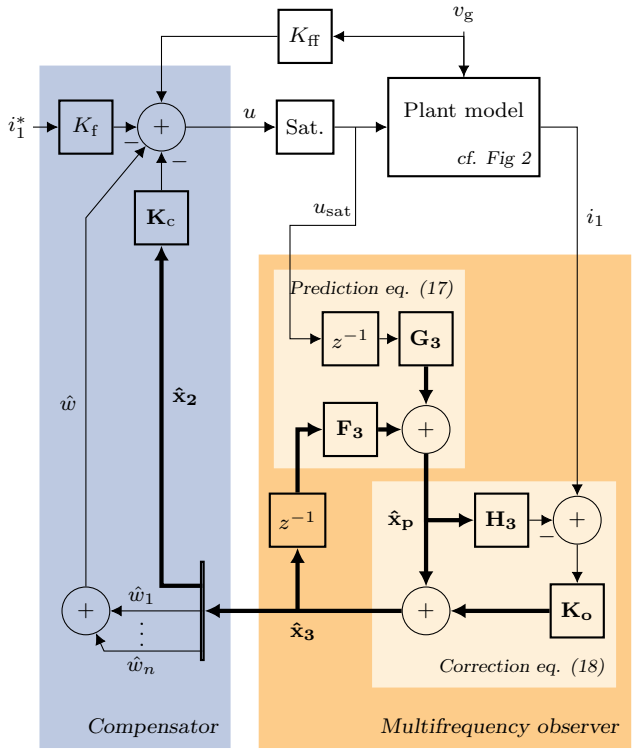

Fig. 3. Proposed multi-frequency grid-side current controller in the $\alpha\beta$ frame.

The resultant discrete multi-frequency disturbance model is

$$\begin{aligned}\mathbf{r}(k+1) &= \mathbf{F_d}\mathbf{r}(k)\\ w(k) &= \mathbf{H_d}\mathbf{r}(k).\end{aligned} \tag{12}$$

Finally, the complete system model is obtained by augmenting the plant model (5) with the input disturbance model (12):

$$\underbrace{\begin{bmatrix}\mathbf{x}_2(k+1)\\ \mathbf{r}(k+1)\end{bmatrix}}_{\mathbf{x}_3(k+1)} = \underbrace{\begin{bmatrix}\mathbf{F_2} & \mathbf{G_2H_d}\\ \mathbf{0} & \mathbf{F_d}\end{bmatrix}}_{\mathbf{F_3}}\underbrace{\begin{bmatrix}\mathbf{x}_2(k)\\ \mathbf{r}(k)\end{bmatrix}}_{\mathbf{x}_3(k)} + \underbrace{\begin{bmatrix}\mathbf{G_2}\\ \mathbf{0}\end{bmatrix}}_{\mathbf{G_3}} u(k)$$

$$i_1(k) = \underbrace{\begin{bmatrix}\mathbf{H_2} & \mathbf{0}\end{bmatrix}}_{\mathbf{H_3}}\underbrace{\begin{bmatrix}\mathbf{x}_2(k)\\ \mathbf{r}(k)\end{bmatrix}}_{\mathbf{x}_3(k)}$$

$$\mathbf{x}_3(k) = \begin{bmatrix}\mathbf{x}_2{}^{\mathrm{T}} & w_{h_1} & w_{h_2} & \cdots & w_{h_n}\end{bmatrix}^{\mathrm{T}}. \tag{13}$$

This augmented model adds to the plant model a resonant action $\mathbf{r}$, which is applied at the plant input. This model is used in the next section to develop the proposed observer, which estimates the plant state $\mathbf{x_2}$ and the required input-equivalent voltage disturbance w that results in zero steady-state error in the grid-side current at the design-selected frequencies.

III. Structure and Design of the Controller

The proposed controller (cf. Fig. 3) aims to control the positive and negative sequences of the fundamental and the typical low-order harmonics of the grid current. The proposed controller structure, cf. Fig. 3, contains two main parts: a compensator and a multifrequency observer. Additionally, a saturator and a grid voltage feedforward is also included. The grid voltage feedforward ensures a bumpless start and improves the response to voltage sags. The saturator provides to the observer a more accurate value of the VSC output voltage when overmodulation occurs. With such controller structure, the wind-up problem is avoided by feeding back the saturated control signal u_{sat} to the observer rather than the control output u because the estimated states are correct and the consistency between the observer and the real plant states is maintained. This eliminates wind-up problems in the observer when the VSC is commanded with a reference that cannot be achieved [22], [30].

In order to carry out the design of the compensator and the observer, the principle of separation of estimation and control is applied. In this manner, the design of the observer and the design of the compensator are performed independently and, when combined, they keep their properties [30].

In view of this, on the one hand, the compensator is designed to provide a good transient response to reference changes. A damped response to reference commands equivalent to a first-order system is obtained due to the adopted direct discrete-time pole-placement strategy. The bandwidth that can be achieved is only limited by the sampling rate and the available bandwidth in the physical system (where overmodulation does not occur, cf. [31, Sec. III-A]).

On the other hand, the observer calculates the estimated plant state vector $\hat{\mathbf{x}}_\mathbf{3}$ using the measured grid-side current i_1 and the saturated controller output voltage u_{sat}. The proposed design provides a good robustness against changes in the grid impedance, as explained in Section IV, and removes the effect of grid voltage disturbances by providing zero steady-state error in the grid-side current at a set of design-selected frequencies.

The compensator contains two gains, namely, a feedback gain $\mathbf{K}_\mathrm{c}$ and a reference feedforward gain K_f. The proposed design method to obtain these two gains uses a direct discrete-time pole-placement strategy which only depends on the resonant frequency of the LCL filter f_{res}, the sampling period of the digital controller T_s, and the desired reference-tracking bandwidth f_{dom}. In the following, the required steps to obtain both gains are detailed.

First, the proposed closed-loop poles of the plant are computed according to [22, Table I]. Then, Ackermann's formula is applied to compute the gain $\mathbf{K}_\mathrm{c}$ that yields a closed-loop system with the specified closed-loop poles:

$$\mathbf{K}_\mathrm{c} = \begin{bmatrix}0 & 0 & 0 & 1\end{bmatrix}\begin{bmatrix}\mathbf{G_2} & \mathbf{F_2G_2} & (\mathbf{F_2})^2\mathbf{G_2} & (\mathbf{F_2})^3\mathbf{G_2}\end{bmatrix} A_{\mathrm{cl}}(\mathbf{F_2}),$$

where A_{cl} is the characteristic polynomial, whose roots are the desired closed-loop poles of the system. The expression of A_{cl} evaluated at $\mathbf{F_2}$ is

$$A_{\mathrm{cl}}(\mathbf{F_2}) = (\mathbf{F_2} - p_1^{\mathrm{cl}}\mathbf{I_4})(\mathbf{F_2} - p_2^{\mathrm{cl}}\mathbf{I_4})(\mathbf{F_2} - p_3^{\mathrm{cl}}\mathbf{I_4})\mathbf{F_2}.$$

When the feedback path is closed using the previously calculated feedback gain $\mathbf{K}_\mathrm{c}$, cf. Fig. 3, the resultant closed-loop system is

$$\begin{aligned}\mathbf{x}_2(k+1) &= \overbrace{(\mathbf{F_2} - \mathbf{G_2K_c})}^{\mathbf{F_{cl}}}\mathbf{x}_2(k) + K_\mathrm{f}\mathbf{G_2}i_1^*(k)\\ i_1(k) &= \mathbf{H_2}\mathbf{x}_2(k).\end{aligned} \tag{14}$$

This article has been accepted for publication in a future issue of this journal, but has not been fully edited. Content may change prior to final publication. Citation information: DOI 10.1109/TIA.2018.2829459, IEEE Transactions on Industry Applications

Such system has the following closed-loop transfer function from its reference $i_1^*(k)$ to its output $i_1(k)$:

$$T(f) = K_{\mathrm{f}}\mathbf{H_2}(e^{j2\pi f T_{\mathrm{s}}}\mathbf{I_4} - \mathbf{F}_{\mathrm{cl}})^{-1}\mathbf{G_2}. \tag{15}$$

In order to achieve unity gain at the nominal grid frequency, e.g., $T(f_{\mathrm{g}}) = 1$, the feedforward gain K_{f} is

$$K_{\mathrm{f}} = \frac{1}{\mathbf{H_2}(e^{j2\pi f_{\mathrm{g}} T_{\mathrm{s}}}\mathbf{I_4} - \mathbf{F}_{\mathrm{cl}})^{-1}\mathbf{G_2}}. \tag{16}$$

This concludes the design of the compensator.

Concerning the design of the observer, now the system model in (13) has a high order. Consequently, it is not easy to design the observer as in [22] (a Luenberger observer with direct discrete-time pole placement) and achieve a robust system, as further explained in Section IV. In order to avoid this problem and simplify the design process, a Kalman filter [30] is used in this article.

The Kalman filter consists of the following two equations. The first one is a prediction equation that estimates the state $\hat{\mathbf{x}}_{\mathbf{3}}(k)$ based on the previous state estimate $\hat{\mathbf{x}}_{\mathbf{3}}(k-1)$ and the last actuation on the plant $u_{\mathrm{sat}}(k-1)$:

$$\hat{\mathbf{x}}_{\mathbf{p}}(k) = \mathbf{F_3}\hat{\mathbf{x}}_{\mathbf{3}}(k-1) + \mathbf{G_3}u_{\mathrm{sat}}(k-1). \tag{17}$$

The second one is a correction equation that modifies this prediction $\hat{\mathbf{x}}_{\mathbf{p}}(k)$ based on the most recent measurement of the grid-side current $i_1(k)$:

$$\hat{\mathbf{x}}_{\mathbf{3}}(k) = \hat{\mathbf{x}}_{\mathbf{p}}(k) + \mathbf{K_o}[i_1(k) - \mathbf{H_3}\hat{\mathbf{x}}_{\mathbf{p}}(k)] \tag{18}$$

where $\mathbf{K_o}$ is the Kalman gain.

This constant gain can be obtained in two different ways: by calculating its analytic expression [29] or by executing an iterative algorithm. Due to its simplicity, the authors recommend using the algorithm given in Appendix A.

In order to calculate $\mathbf{K_o}$, two parameters need to be defined: the measurement (or sensor) noise N and the process (or plant) noise $\mathbf{Q}$. The first parameter, N, can be easily obtained from the grid-side current measurement i_1 when the VSC is on and disconnected from the grid:

$$N = \mathcal{E}\{|i_1(k)|^2\} \tag{19}$$

where $\mathcal{E}\{\circ\}$ denotes mathematical expectation [30] and can be approximated by a time average of its argument. The second parameter, the process noise $\mathbf{Q}$, represents the uncertainty in the system model and disturbances. The relation between N and $\mathbf{Q}$ determines the bandwidth of the observer. A higher observer bandwidth is obtained if N is reduced (the grid-side current measurements are accurate) or if $\mathbf{Q}$ is increased (the disturbances vary a lot, e.g., the amplitude of voltage harmonics changes quickly). In the next section, the effect of $\mathbf{Q}$ is analyzed and a value for this parameter is proposed. The details for computing the Kalman gain $\mathbf{K_o}$ using N and $\mathbf{Q}$ are given in Appendix A. The computational complexity of the control algorithm depending on the number of controlled harmonics is analyzed in detail in Appendix B. This study shows that the computational load of the control algorithm is suitable for an implementation using a microcontroller.

IV. Performance Analysis of the Proposed Controller

The observer proposed in the previous section can, theoretically, eliminate as many harmonics as desired because the number n of frequencies where a resonant action (infinite gain) [22] can be placed is not limited. The only obvious practical limitation is the computational burden. In any case, current processors can execute the proposed control equations, which consist only of simple additions and multiplications (cf. Fig. 3 and Appendix B), without any problems even for large orders [cf. (13)]; hence, this constraint is virtually eliminated. Unfortunately, the disturbance rejection capability and the robustness of the grid-tied inverter is restricted by some fundamental limitations that are common to all linear controllers. In the following, these fundamental constraints are analyzed. A good understanding of them also helps to evaluate and choose a convenient value of $\mathbf{Q}$.

First a qualitative analysis, using the sensitivity function, of the tradeoffs involved in the design of the multi-frequency observer is presented in Section IV-A. Then, in Section IV-B, a quantitative analysis that relates $\mathbf{Q}$ with the position of the system poles is adopted to solve such tradeoffs. Finally, the advantage of the adopted reference-input structure (state-command) over the reference-input structure typically used with resonant controllers (output-error command) is studied in Section IV-C.

A. Sensitivity Function of the System

The sensitivity function $S(f)$ of the system shows how the controller responds to disturbances [30]. It indicates how much the controller modifies (amplifies or attenuates) the effect of disturbances (e.g., the grid voltage v_g, VSC nonlinearities, and plant model mismatches) on the grid-side current with respect to the open-loop response. The calculation process to obtain $S(f)$ is given in Appendix C.

Under normal operating conditions [3], the orders of the larger-amplitude harmonics in the per-phase grid voltage are $3, 5, 7, 9, 11$, and 13. In addition, the harmonic orders associated to the VSC nonlinearities coincide with those of the grid [32]. These voltage disturbances, under balanced conditions, correspond to the harmonic orders $h = -5, +7, -11$, and $+13$ in the $\alpha\beta$ frame. The third and ninth harmonics are mapped to the zero-sequence component, and they do not cause any current circulation in a balanced or three-wire system. Furthermore, the negative sequence of the fundamental grid voltage ($h = -1$) should also be included in the disturbance model. The reason is that, although the unbalance of the fundamental component shall be within the range 0% to 3% during normal operation [3], it can be significantly bigger and become the main voltage disturbance under a fault condition, such as a voltage sag [3].

In this manner, a multi-frequency controller achieves zero sensitivity $S(f)$ at a set of arbitrarily specified frequencies $[\,S(f_g h_1) = S(f_g h_2) = \cdots = S(f_g h_n) = 0\,]$, so as to eliminate the distortion, and a low sensitivity at the resonant frequency of the LCL f_{res}, in order to improve the lack of attenuation of the LCL filter around this frequency region and

This article has been accepted for publication in a future issue of this journal, but has not been fully edited. Content may change prior to final publication. Citation information: DOI 10.1109/TIA.2018.2829459, IEEE Transactions on Industry Applications

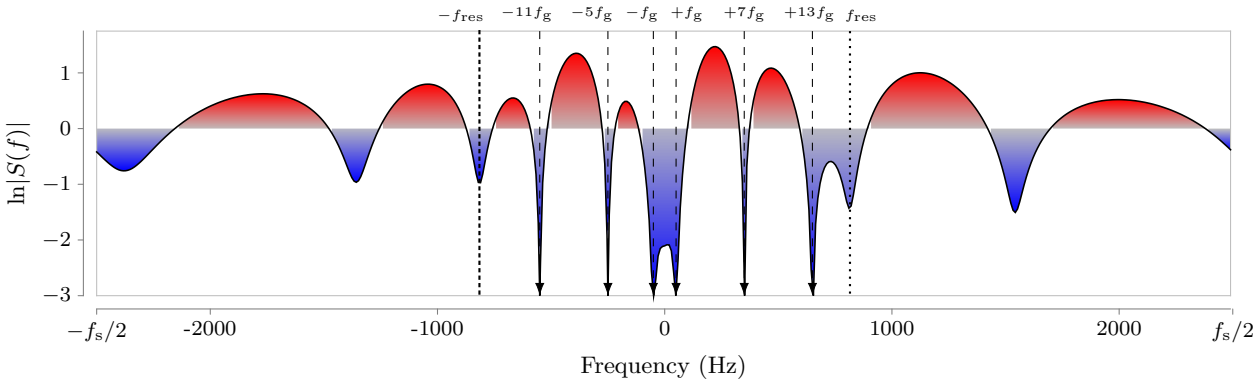

Fig. 4. Graphical interpretation of the Bode integral [cf. (20)], for a multi-frequency controller, that shows a restriction that applies to the sensitivity function. In this example, the controller uses a Luenberger observer with dynamics that are twice as fast as the dominant pole of the compensator [22].

damp the resonance. Fig. 4 shows $\ln|S(f)|$ when f_s is 10 kHz and the harmonics $+1, -1, -5, +7, -11, +13$ are controlled. This is accomplished by placing observer open-loop poles at the desired frequencies [cf. (9)] in conjunction with the model of the plant, [cf. (5)], as done in (13). In the following, it is shown that if the number of harmonics controlled with zero steady-state error augments (n increases), then the sensitivity of the system at other frequencies is amplified. Therefore, the aforementioned set of main harmonic orders correspond to the frequencies among which the low-sensitivity regions of the controller should be distributed in order to maximize the performance.

The sensitivity function must satisfy two requirements [33]: an analytic and an algebraic design tradeoff. The first requirement (the analytic design tradeoff) states that, in the case of a system model with no open-loop poles outside the unit circle, such as (13), the average attenuation and amplification of disturbances over the complete frequency range where the controller operates $(-f_s/2, f_s/2)$ is zero, where f_s is the sampling frequency:

$$\int_{-f_s/2}^{f_s/2} \ln|S(f)|\, df = 0. \tag{20}$$

Thus, the choice of the sensitivity function $S(f)$ at one frequency affects its value at other frequencies. This effect is illustrated in Fig. 4. The area above the curve must be equal to the area below the curve according to (20). Consequently, if the designer increases the number of frequencies with low sensitivity (to cancel more harmonics), the sensitivity at other frequencies also increases.

To try to overcome the previous constraint, a higher sampling rate f_s could be used. If the frequency band where the integration is performed widens, the new frequency region could be used to spread the area associated to sensitivities greater than one and yield a lower peak magnitude of the sensitivity function. Therefore, a double-update strategy is recommended because it increases f_s, compared to a conventional single-update strategy, and maintains the same switching frequency. Unfortunately, this approach (increasing f_s) cannot be used indefinitely. There is no significant improvement in sampling faster than a certain frequency, because of the second requirement, as explained next.

The second requirement (the algebraic design tradeoff) states that the sensitivity function $S(f)$ and the complementary sensitivity function $T(f)$ are related at all frequencies [30]:

$$S(f) + T(f) = 1. \tag{21}$$

The complementary sensitivity function $T(f)$ is the transfer function that relates the grid-side current i_1 with its reference i_1^* when an output-error feedback structure is used. The calculation process to obtain $T(f)$ is given in Appendix C. This transfer function should be close to zero for frequencies above the resonant frequency of the LCL filter, due to the low-pass behavior of the plant (the LCL filter); otherwise, a high controller effort would be required, which would cause overmodulation in the VSC. From (21), as $T(f)$ approaches zero, $S(f)$ must approach one [i.e., $\ln|S(f)|$ goes to zero]. Therefore, although the designer could be tempted to spread the area with sensitivity greater than one in Fig. 4 over a wide frequency range up to $\pm f_s/2$ to reduce the sensitivity peak, in reality this compensation has to take place in a narrower bandwidth, as $\ln|S(f)|$ must be close to zero beyond the available bandwidth (the resonant frequency of the LCL filter) of the closed-loop system.

There is another important reason to avoid spreading the red area (sensitivities greater than one) over high frequencies. The sensitivity function describes how much the controller modifies (amplifies or attenuates) the effect of disturbances. In order to achieve this control action, the controller relies on the system model. Nevertheless, this model usually presents deviations from the real plant, which are especially significant at high frequencies, where unmodeled dynamics are more common. Therefore, if the controller responds to disturbances in such frequency ranges (i.e., the red area extends to high frequencies), then the resultant system presents a greater sensitivity to plant and parameter variations.

B. System Sensitivity With a Luenberger Observer and With a Kalman Filter

Section IV-A has presented two restrictions that the sensitivity function has to meet. These restrictions limit the

This article has been accepted for publication in a future issue of this journal, but has not been fully edited. Content may change prior to final publication. Citation information: DOI 10.1109/TIA.2018.2829459, IEEE Transactions on Industry Applications

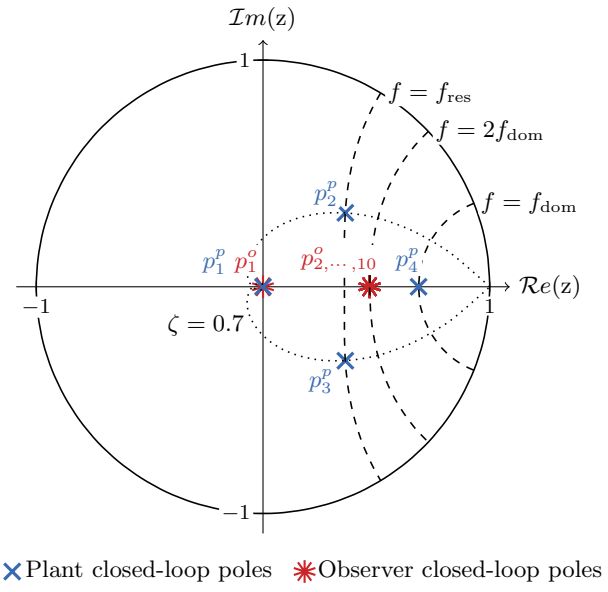

Fig. 5. Closed-loop poles of the system using a direct discrete-time pole-placement strategy (a Luenberger observer).

performance of the controller by imposing a tradeoff between the disturbance-rejection capability and the sensitivity of the system to parameter variations. In what follows, the previous fundamental constraints are analyzed when a Luenberger observer or a Kalman filter are used. In the case of the Kalman filter, the effect of the process noise parameter $\mathbf{Q}$ on the observer poles and on the system sensitivity is shown.

Conventionally, the design of the observer is carried out using frequency-domain techniques and the dynamics of the observer are usually faster than those of the compensator [29]. Nonetheless, although this frequency-domain design approach is convenient when a small and fixed number of frequencies are controlled, it can result in a bad design in terms of robustness when applied to a multi-frequency controller.

The physical explanation of this problem that occurs with a conventional design is as follows. When a complicated (high-order) voltage disturbance is estimated, unmodeled disturbances in the grid-side current measurements and plant parameter variations cause greater error in the estimation; therefore, a larger sensitivity is obtained. This problem is further illustrated and analyzed in the next example.

Fig. 4 shows the sensitivity function of a controller designed for the system parameters that are used in the experimental setup (cf. Table I). The harmonics $+1, -1, +7, -5, +13, -11$ are controlled with zero steady-state error with a Luenberger observer that is designed using the criteria included in [22], which are based on the frequency domain. The system has fourteen closed-loop poles: four poles related to the plant model of the compensator $p_{1,\cdots,4}^p$ and ten observer poles $p_{2,\cdots,10}^o$ (four from the plant model and six from the disturbance model). The observer poles are placed at twice the frequency of the dominant pole p_4^p (cf. Fig. 5) [22]. These closed-loop pole locations give a high sensitivity (red areas in Fig. 4) at frequency ranges above the resonant frequency, which yields a low robustness. Another inconvenient is the presence of useless low-sensitivity areas outside the targeted frequencies, which contribute to worsen the performance at other frequencies. An optimum sensitivity function should have sensitivities lower than unity only at the frequency regions of the targeted harmonics and at the resonant frequency of the LCL filter. In addition, the sensitivities greater than one should be spread evenly in the rest of the frequency range where the controller operates, i.e., below the cut off frequency of the LCL filter. From the previous example it is clear that a better closed-loop pole-placement strategy is needed when a multi-frequency controller is considered.

Instead of designing the observer according to its dynamic characteristics, which results in a high sensitivity, a time-domain approach that minimizes the estimation error is adopted. This method is particularly useful in this case, where a multi-frequency observer is considered, because it frees the designer from defining the multiple required closed-loop pole locations. In this manner, $\mathbf{K_o}$ is selected to give estimates of the plant state $\hat{\mathbf{x}}_\mathbf{2}$ and the grid voltage $\hat{w}$ that minimize the estimation error under some assumptions. The Kalman filter (cf. Fig. 3) is a solution to this minimization problem. This filter minimizes the mean square error of the estimated state vector $\hat{\mathbf{x}}_\mathbf{3}$ assuming that the unmodeled disturbances that affect the plant $\mathbf{Q}$ and the measurement noise of the sensors N are random and of a certain mean square value. If these two assumptions are valid, then the proposed solution (the Kalman filter) is also optimal. The uncertainty about the characteristics of the grid voltage, the plant parameters, and the converter nonlinearities prevents from having the true N and $\mathbf{Q}$ values accurately and obtaining the optimal solution. Nevertheless, in application of the central limit theorem [34], the combined result of all the small remaining unmodeled effects (e.g., plant model mismatches and other small voltage harmonics) can be described as random. Therefore, the previous two assumptions are a reasonable approximation to describe all the aforementioned uncertainties without resorting to a complex nonlinear time-variable model. The process noise parameter $\mathbf{Q}$ assigns a quantitative value to all these unmodeled effects. The effect of $\mathbf{Q}$ is further illustrated in the following.

Fig. 6 shows the sensitivity function of the proposed controller (cf. Fig. 3) designed for the system parameters that are used in the experimental results (cf. Table I). This sensitivity function achieves a better (compared to Fig. 4) distribution of the low- and high-sensitivity frequency regions. In this manner, a more robust system to plant variations, namely, the grid impedance and the LCL filter parameters, is also obtained. In the following, the proposed Kalman filter is further analyzed and a value of $\mathbf{Q}$ is recommended.

Fig. 7(a) shows the closed-loop roots of the sensitivity transfer function $S(f)$ for a sweep in the process noise $\mathbf{Q}$. When $\mathbf{Q}$ increases, the observer closed-loop poles move away from the disturbance zeros. Conversely, as $\mathbf{Q}$ approaches zero, the poles get closer to the disturbance zeros. The Kalman filter reallocates the rest of the observer zeros so as to yield an optimal sensitivity function for the values of N and $\mathbf{Q}$ provided. A detail of their effect on the magnitude is shown

This article has been accepted for publication in a future issue of this journal, but has not been fully edited. Content may change prior to final publication. Citation information: DOI 10.1109/TIA.2018.2829459, IEEE Transactions on Industry Applications

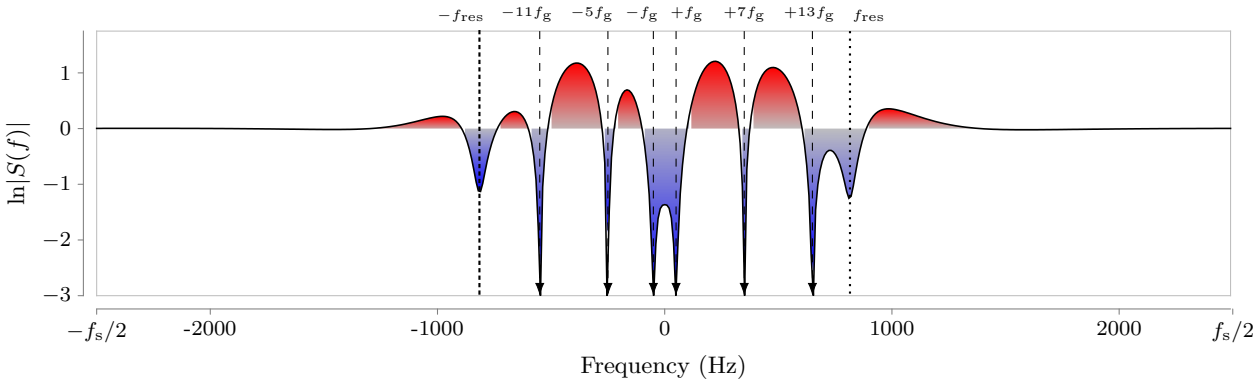

Fig. 6. Graphical interpretation of the Bode integral for the proposed multi-frequency controller.

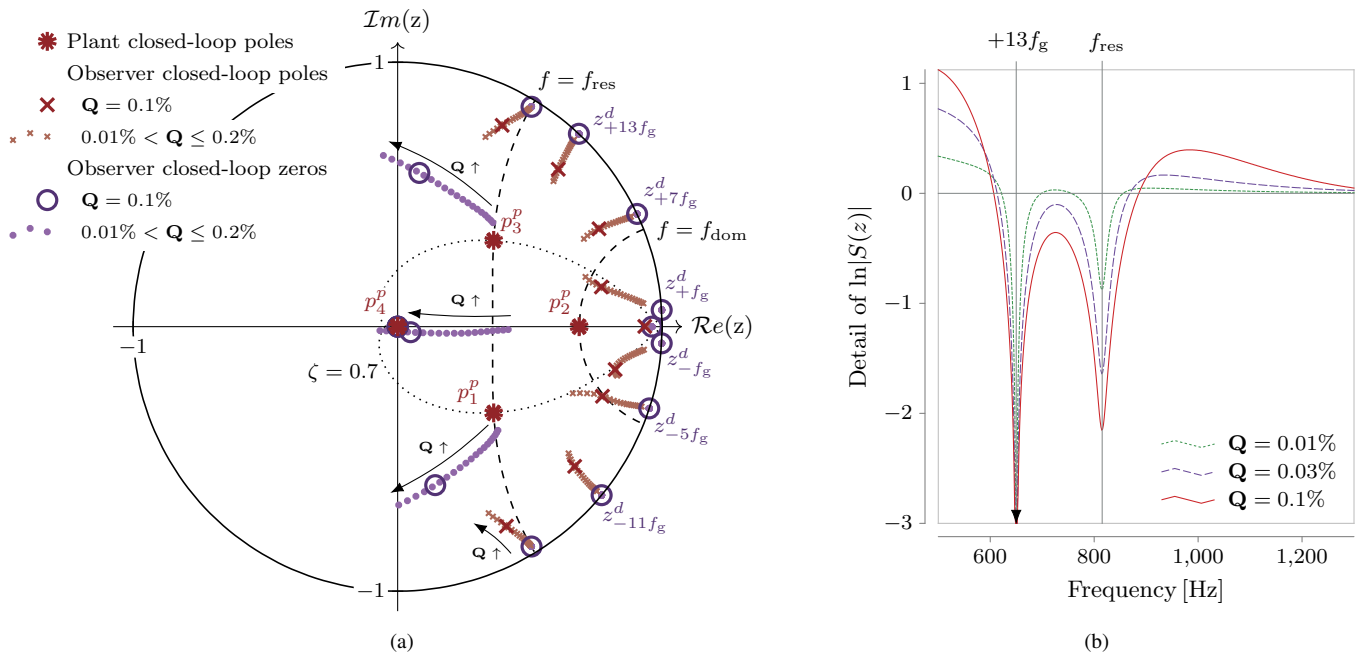

Fig. 7. Sensitivity function $S(f)$ using a Kalman filter in the observer, and a direct discrete-time pole-placemente strategy [22] to design the compensator. (a) Closed-loop poles and zeros. (b) Detail of the magnitude at one of the controlled harmonics (+13) and at the resonant frequency of the LCL filter.

in Fig. 7(b). The value of $\mathbf{Q}$ is changed from 0.01% to 0.2%. The bandwidth of a multi-frequency observer is determined by the width of the low-sensitivity regions around the frequencies of interest (cf. Fig. 6). Wide low-sensitivity frequency regions eliminate the targeted disturbances fast. The Kalman observer automatically adjusts the bandwidth of the observer (depending on the values of N and $\mathbf{Q}$ provided) by controlling the distance between the closed-loop poles of the observer and the zeros associated to the disturbances rejected with zero-steady state error, i.e., the disturbance zeros z_h^d. Based on the results of this analysis, a value of 0.1% is here recommended to be used in the design. This value can be modified from the proposed one to improve the performance depending on the particular conditions where the VSC is installed. If, e.g., the voltage fluctuates significantly (at the fundamental or at harmonic frequencies) a higher value of $\mathbf{Q}$ is recommended. Conversely, if the VSC is connected to a weak grid (the plant parameters vary significantly from the nominal model), then a lower $\mathbf{Q}$ yields a more robust controller.

Furthermore, the plant closed-loop poles $p^p_{1,2,3,4}$ do not move, as expected from the pole-placement strategy adopted for the compensator [22]. This permits to obtain a constant reference-tracking performance irrespectively of the number of harmonics controlled and the bandwidth selected for the observer. A detailed analysis concerning this fact is given in Section IV-C.

Finally, it is important to notice that the proposed controller and the limitations presented do not depend on the LCL filter values because the design takes into account the parameters of the plant to be controlled. The described solution can operate with a resonant frequency of the LCL filter above or below $f_s/6$, i.e., the threshold above which conventional controllers have stability problems [26]. The achievable performance depends on the measured value of N (sensor noise) and the

This article has been accepted for publication in a future issue of this journal, but has not been fully edited. Content may change prior to final publication. Citation information: DOI 10.1109/TIA.2018.2829459, IEEE Transactions on Industry Applications

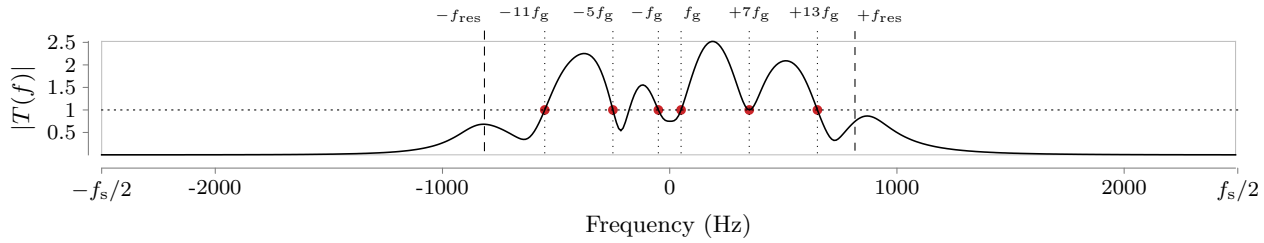

Fig. 8. Magnitude of the complementary sensitivity function $T(f)$ (the transfer function that relates the current reference input i_1^* to the grid-side current reference i_1) when an output-error-command structure is used in a multi-frequency controller designed with the proposed Kalman observer.

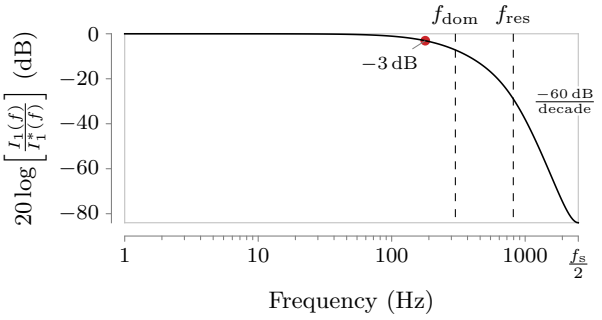

Fig. 9. Magnitude of the transfer function that relates the current reference input i_1^* to the grid-side current reference i_1 when a state-command structure is used in a multi-frequency controller designed with the proposed Kalman observer.

selected value of $\mathbf{Q}$ (process noise), which should be selected in accordance with the amount of unmodeled disturbances that the current controller has to deal with.

C. Analysis of the Reference-Tracking Performance of the Proposed Multi-Frequency Controller

The transfer function from the current reference i_1^* to the grid-side current i_1 is determined by the reference input structure selected. This section analyzes the advantage of the state-command structure (the adopted solution) for a multi-frequency current controller over the traditional output-error feedback. The output-error feedback structure is typically used in classic transfer-function design [11], [17], [21], where the controller transfer function is driven by an error signal $e = i_1 - i_1^*$.

On the one hand, when an output-error feedback is chosen, the reference-to-output transfer function is the complementary sensitivity function $T(f)$ (cf. Fig. 8). This transfer function has unity gain at the frequencies controlled with zero steady-state error; however, it does not have a flat frequency response. In the particular case of a multi-frequency controller, there are several closed-loop poles at low frequencies [the observer poles in a state-space controller, cf. Fig. 7(a), or the controller poles in a classic transfer-function design] that significantly degrade the transient response to reference commands (non flat frequency response, cf. Fig. 8). Depending on the harmonics controlled, the response would also vary because the denominator of this transfer function includes the closed-loop poles of the observer [cf. Fig. 7(a)] or the closed-loop poles of the controller transfer function in a classic design.

On the other hand, if a state-command structure is used, the reference-to-output transfer function is not $T(f)$. Now the transfer function only contains the closed-loop poles of the plant, irrespectively of the number of harmonics controlled [29]. Hence, this transfer function has a flat frequency response below the cutoff frequency (cf. Fig. 9), as expected from the plant closed-loop pole locations [22], and mainly determined by the dominant pole. The cutoff frequency ($-3\,\text{dB}$) is slightly smaller than f_{dom} due to the effect of the other three non-dominant closed-loop poles of the plant. In this manner, contrarily to a conventional resonant controller, the state-command structure does not modify or degrade the reference-tracking capability, irrespectively of the order of the observer [30]. Therefore, this reference-input structure presents an increasing advantage over the traditional solution as the number of harmonics controlled n augments.

V. Robustness to Grid Impedance Variations

The analysis presented in the previous section explains how the design process determines the achieved robustness. As explained, in order to obtain a high robustness, the control action should be focused only at the frequencies where disturbances are expected, namely, low-order grid-frequency harmonics. However, the previous theoretical analysis does not indicate the range of grid impedance values where the controller can operate. In this section, a numerical analysis is carried out to evaluate the stability of the controller for a wide range of grid impedance values.

The stability is assessed by calculating the time constant of the poles of the closed-loop system when the grid impedance is increased. The time constant (or decay time-constant) of a pole at frequency f and damping ratio ζ is $\tau = 1/(2\pi f\zeta)$.

In the case of a weak grid, the robustness of the controller can be modified depending on the feedforward gain implemented [35]. Since the proposed controller does not rely on a voltage feedforward to achieve stability, the analysis presented in this section was performed assuming that K_{ff} is zero so as to study the robustness of the current controller isolated from such effect.

Fig. 10 shows regions of grid impedance, whose colors denote the value of the largest time constant $\tau_{\max}$ in the system, that is, the time constant of the pole with the slowest dynamics. The relation between each color and its corresponding time

This article has been accepted for publication in a future issue of this journal, but has not been fully edited. Content may change prior to final publication. Citation information: DOI 10.1109/TIA.2018.2829459, IEEE Transactions on Industry Applications

TABLE I
EXPERIMENTAL SETUP PARAMETERS

Base values		
Nominal power	P_{base}	10 kW
Phase voltage	V_{base}	230 V
Nominal current	I_{base}	14.5 A
Grid frequency	f_{g}	50 Hz
LCL filter		
Grid-side inductance	L_1	2.5 mH (5 %)
Converter-side inductance	L_2	2.5 mH (5 %)
Filter capacitance	C	30 μF (14 %)
Filter resonance	f_{res}	815 Hz
Weak grid		
Grid inductance	L_{g}	5.4 mH (10 %)
Grid resistance	R_{g}	2.5 Ω (15 %)
VSC		
Switching frequency		2.5 kHz
Dead time		3 μs
DC-bus voltage	v_{dc}	750 V
Controller		
Sampling frequency	f_{s}	5 kHz
Dominant frequency	f_{dom}	300 Hz
Measurement noise	N	0.01 A^2
Process noise	$\mathbf{Q}$	0.1%

constant interval is indicated in the label at the right of the figure. Both the resistive and the reactive components of the grid impedance (R_{g} and L_{g} respectively) are changed from zero to a value of 1 p.u., cf. base values in Table I. Three different values of the design parameter $\mathbf{Q}$ are tested, namely, the recommended value of $0.1\,\%$ (cf. Section IV-B) and the two limit values shown in Fig. 7(a) ($0.2\,\%$ and $0.01\,\%$).

When $\mathbf{Q}$ is set to $0.01\,\%$ [low bandwidth, cf. Fig. 10(a)], the resultant design has a slower response to disturbances compared to the recommended value of $\mathbf{Q} = 0.1\,\%$ due to its larger time constant under nominal conditions ($R_{\text{g}} = L_{\text{g}} = 0$). Nevertheless, this design has a high robustness and is always stable in spite of changes in the grid impedance value ($R_{\text{g}}, L_{\text{g}} \leq 1$ p.u.).

If $\mathbf{Q}$ is set to $0.1\,\%$ (recommended bandwidth), a faster rejection of disturbances is obtained under nominal conditions ($Z_{\text{g}} = 0$ p.u.). However, $\tau_{\max}$ increases faster, compared to the previous case, as the grid short circuit ratio (SCR) is increased, cf. Fig. 10(b). In particular, $\tau_{\max}$ doubles when the inverter is tied to a weak grid with impedance $Z_{\text{g}} = 0.15 + j0.1$ p.u., cf. Table I. Nevertheless, the controller remains stable for values of the grid inductance L_{g} smaller than 0.8 p.u., cf. Fig. 10(b). When the grid impedance becomes greater than such a large value, e.g., during islanded operation, a voltage controller should be used in place of a current controller.

Finally, when $\mathbf{Q}$ is set to $0.2\,\%$, no further improvements are obtained under nominal conditions. Nevertheless, the obtained grid-impedance region with a time constant smaller than 20 ms is smaller than in the previous case because the system is less robust to changes in the plant parameters.

VI. EXPERIMENTAL AND SIMULATION RESULTS

The proposed multi-frequency controller is tested in a VSC working as an inverter connected to a three-phase grid. A three-phase ac voltage source was used so as to generate the distorted grid voltage and the voltage sags. The switching frequency is 2.5 kHz and a double-update scheme is used, yielding a sampling frequency of $f_{\text{s}} = 5$ kHz. Such low switching frequency reduces switching losses in the VSC and it represents a worst-case scenario in terms of the effect of the computation and modulation delays. The setup parameters are summarized in Table I. The LCL filter was designed according to [36], resulting in a high-performance filter with reduced reactive values. The grid voltage has the harmonics presented in Table II and a total harmonic distortion (THD) of 10.5%. The controller was designed according to the proposed method. The phase-locked loop (PLL) presented in [37] is used. Figs. 11(a) and 11(b) show a diagram and a photograph of the experimental setup, respectively.

The first test shows the effect of the resonant action of the observer. If $\hat{w}$ is zero in the control law (cf. Fig. 3), the resonant action of the observer is stopped. Fig. 12(a) shows the effect of enabling $\hat{w}$ in the controller. Fig. 12(b) displays the grid-side current spectrum before and after the activation of $\hat{w}$. As expected, when the resonant action is enabled, zero steady-state error is obtained at the controlled harmonics.

In the second test, the reference-tracking capability of the VSC is evaluated. Fig. 13(a) shows a reference step $i^*_{1,dq}$ in the positive-sequence dq frame (dq+ frame). The measured grid-side current $i_{1,abc}$ is transformed into the synchronous dq+ frame obtaining $i_{1,dq}$. Contrarily to the abc representation, the dq profiles allow to easily visualize the rise time, settling time, overshoot, steady-state error, and axis cross coupling in the response of the current controller. The 10%–90% rise time is approximately 1.5 ms, as expected from the bandwidth of the system [$T_{10\%-90\%} = \ln|9|/(2\pi f_{\text{dom}}) = 1.2$ ms]. This is in accordance with [22], where a f_{dom} of 150 Hz (and other LCL filter) was used and a rise time of 2.5 ms was obtained. In addition, negligible overshoot and good axis decoupling is attained because the response is not affected by the observer poles, as intended.

Fig. 13(b) shows the spectrum of the grid-side current $i_1(f)$ and the grid voltage $v_g(f)$ in the $\alpha\beta$ frame (both axis use a linear scale). As expected, the substantial voltage distortion ($-11, -5, -1, +7, +13$ harmonics) does not cause any current circulation due to the action of the proposed multi-frequency controller.

The third test evaluates the robustness of the controller to sags in the grid voltage. Sags usually cause unbalanced voltage grid conditions. In particular, a 40%-depth type-C sag [38] is generated. The response to voltage sags in different depth can be easily derived because the system is composed of a linear controller and a plant that can be described with a linear model, cf. Fig. 3; therefore, the resultant closed-loop system is also linear. Using the scaling property of linear systems, it can be seen that scaling the input (changing the depth of a voltage sag) scales the output by the same factor. This type of sag contains both fundamental voltage sequences (± 1) in

This article has been accepted for publication in a future issue of this journal, but has not been fully edited. Content may change prior to final publication. Citation information: DOI 10.1109/TIA.2018.2829459, IEEE Transactions on Industry Applications

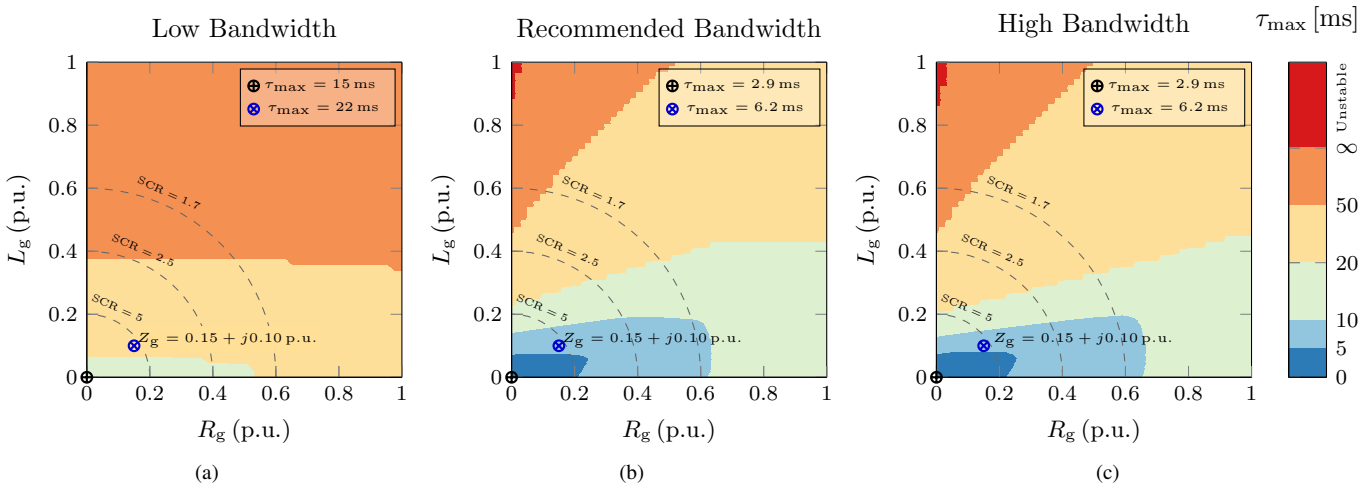

Fig. 10. Stability regions as a function of the grid impedance. (a) Low bandwidth ($Q = 0.01\%$). (b) Recommended bandwidth ($Q = 0.1\%$). (c) High bandwidth ($Q = 0.2\%$).

TABLE II
GRID VOLTAGE PARAMETERS

Order	Sequence*	*h*	Magnitude
1	+	+1	230 V
3	0		5 %
5	−	−5	6 %
7	+	+7	5 %
9	0		1.5 %
11	−	−11	3.5 %
13	+	+13	3 %
THD			10.5 %

* When the sag occurs, the harmonic voltages are unbalanced (all sequences are present for each harmonic).

addition to the harmonics described in Table II. Fig. 14(a) shows the transient response of the current controller to this voltage sag. The current reference $i^*_{1,dq+}$ is kept constant so as to observe the response to the sag isolated from other actions that also cause transients in the grid-side current. A transient time of 10 ms is obtained due to the dynamics of the Kalman observer [cf. the observer poles in Fig 7(a)]. The increase in the disturbance-rejection transient duration (compared to 6 ms in [22]) is an unavoidable limitation, as explained in Section IV, because now six frequencies are being controlled with zero steady-state error instead of just two as in [22]. Notwithstanding, the resulting response is in any case relatively fast.

Fig. 14(b) shows the response in the frequency domain of the controller during the sag (the spectrum starts being measured 15 ms after the sag event to capture the steady-state regime). In this case, due to the unbalanced grid voltage, both positive and negative sequences of the harmonic voltages from Table II arise in the $\alpha\beta$ frame. The controller continues eliminating the targeted disturbances, including the negative sequence of the fundamental (harmonic -1). The new grid-voltage harmonics (-7, $+5$, and ± 3) are associated to the unbalance and are not eliminated; hence, they cause some undesirable current circulation (cf. Fig. 6). This explains the increased error during the sag fault [cf. Figs. 13 and 14]. Of course, the designer could also include these harmonic frequencies in the design and eliminate them, at the expense of increasing the sensitivity at other frequencies, as it has been described in Section IV. Nevertheless, the main voltage harmonics, as well as the fundamental unbalance $v_g(-f_g)$, which is now the most important voltage disturbance, are still rejected with zero steady-state error.

The fourth test shows the effect of modifying $\mathbf{Q}$. Two values of $\mathbf{Q}$ are tested: the recommended value of 0.1% and one an order of magnitude smaller (0.01%). As aforementioned, $\mathbf{Q}$ controls the width of the blue (low sensitivity) frequency regions shown in Fig. 6. In Fig. 15, the grid voltage is changed from a low-distortion situation to the highly-distorted voltage defined in Table II. The transient duration in Fig. 15(b) increases with respect to Fig. 15(a), as expected, because the observer has a lower bandwidth (cf. Fig. 7 and 10).

In order to assess the robustness of the proposal when connected to a weak grid, the fifth and last test shows the operation of the controller under the same conditions as in the third test (a 40%-depth type-C sag with harmonic distortion) but connected to a weak grid. Now the grid has an impedance Z_g with a value of $0.1 + j0.15$ p.u., cf. Table I. This grid impedance value is also denoted with a cross mark in Fig. 10. Such change causes a small reduction of the damping of the system, cf. Fig. 10(b). In particular, when Z_g is $0.1 + j0.15$ p.u., the smallest damping of the system is lower than 0.05 (orange region); whereas, under nominal conditions, the minimum damping is higher than 0.05 (blue region). According to the analysis presented in Section IV, the stability is not lost when the grid impedance is changed. Furthermore, the transient dynamics are not significantly modified, as expected from the small change in the damping of the system. Fig. 16(a) shows the response of the current controller to the previously described voltage sag. A 5-A overshoot in both dq axis is obtained, which is slightly smaller than the the 8-A overshoot measured in the nominal case, see Fig. 14(a).

This article has been accepted for publication in a future issue of this journal, but has not been fully edited. Content may change prior to final publication. Citation information: DOI 10.1109/TIA.2018.2829459, IEEE Transactions on Industry Applications

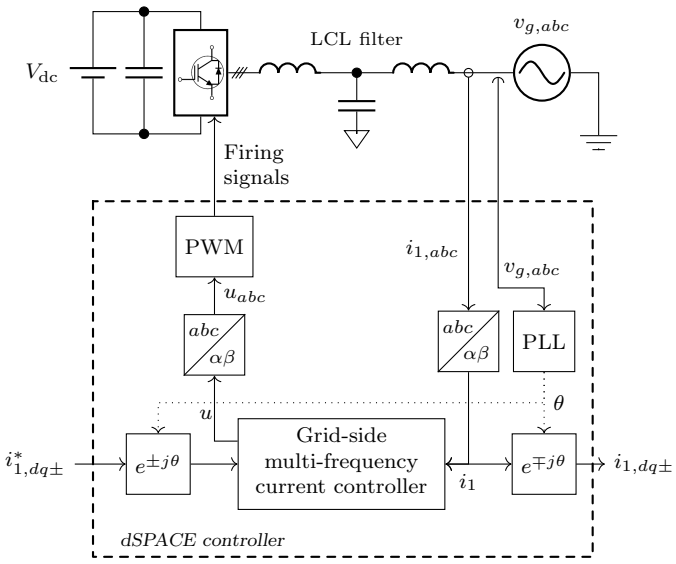

(a)

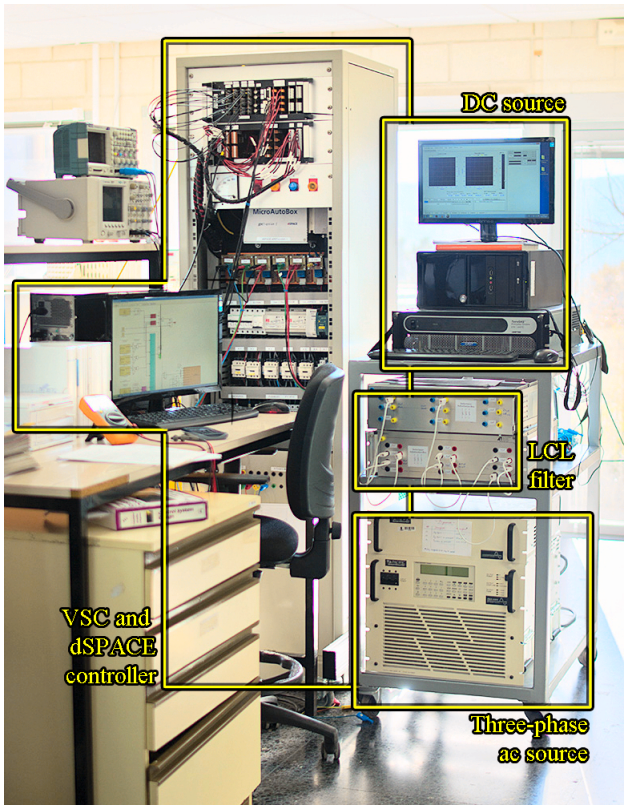

(b)

Fig. 11. Experimental setup. (a) Diagram. (b) Photograph.

Such reduction in the current overshoot is due to the increase in the grid-impedance value, which limits the current during the fault event. Concerning the settling time, both cases show a settling time of approximately 10-ms. An exact value cannot be measured because the uncontrolled unbalanced harmonics that appear during the sag event cause an additional steady-state error. Contrarily to Fig. 14(a), now the measured voltage at the PCC $v_{g,abc}$ contains more switching noise because a voltage divider is formed by the LCL filter and the grid impedance. Therefore, some of the large switching harmonics created by the VSC appear at the PCC. As expected, there is no current circulation at the design selected frequencies in spite of the change in the grid impedance, cf. Fig. 16(b), due to the resonant action of the observer.

VII. Conclusion

This paper has presented a multi-frequency current controller based on a direct discrete-time pole-placement strategy and a Kalman filter for grid-tied converters with LCL filter.

In addition to the advantages of previously proposed harmonic-current controllers, the presented solution responds to commands with a constant, damped, and fast response independently of the LCL filter used or the targeted harmonics. The rise-time value for reference changes is determined by the selected dominant frequency f_{dom} of the compensator.

Concerning the disturbance-rejection capability, the proposed scheme achieves zero steady-state error in the grid-side current at a set of arbitrarily specified harmonic currents. Contrarily to the previously proposed solutions, the controller offers an infinite impedance at these frequencies without altering the response to reference commands or affecting the stability and robustness of the system, when several current harmonics are being controlled.

It has also been shown that the response to disturbances cannot be simultaneously improved in the steady-state operation and during transients. If the number of controlled harmonics increases (to reduce the steady-state error), then the transient response to disturbances of the controller is degraded. This is an unavoidable tradeoff that applies to all linear controllers.

The proposal has also been proved robust against alterations in the grid impedance. Stability is maintained with minimal change in the transient dynamics of the system regardless of the grid-impedance variation.

The design and the theoretical outcomes have been verified by simulations and experiments.

Appendix A
Steady-State Kalman-Filter Gain

In the following, the procedure to calculate the observer gain $\mathbf{K_o}$ (cf. Fig. 3) is detailed.

Since the system model is linear and stationary, the algorithm that calculates the Kalman gain $\mathbf{K_o}$ converges to a steady-state value [30]. The computation of this gain can be performed offline to reduce the computational load of the controller.

A simple iterative numerical solution is shown in Algorithm I. The input parameters of the algorithm are the measurement noise N [cf. (22)]; the process noise $\mathbf{Q}$, for which a value of 0.1% is recommended (cf. Section IV)

$$\mathbf{Q} = \frac{0.1}{100}\begin{bmatrix} I_{\text{base}} & 0 & 0 & 0 & 0 & \cdots & 0 \\ 0 & I_{\text{base}} & 0 & 0 & 0 & \cdots & 0 \\ 0 & 0 & V_{\text{base}} & 0 & 0 & \cdots & 0 \\ 0 & 0 & 0 & V_{\text{base}} & 0 & \cdots & 0 \\ 0 & 0 & 0 & 0 & V_{\text{base}} & \cdots & 0 \\ \vdots & \vdots & \vdots & \vdots & \vdots & \ddots & \vdots \\ 0 & 0 & 0 & 0 & 0 & \cdots & V_{\text{base}} \end{bmatrix}; \quad (22)$$

This article has been accepted for publication in a future issue of this journal, but has not been fully edited. Content may change prior to final publication. Citation information: DOI 10.1109/TIA.2018.2829459, IEEE Transactions on Industry Applications

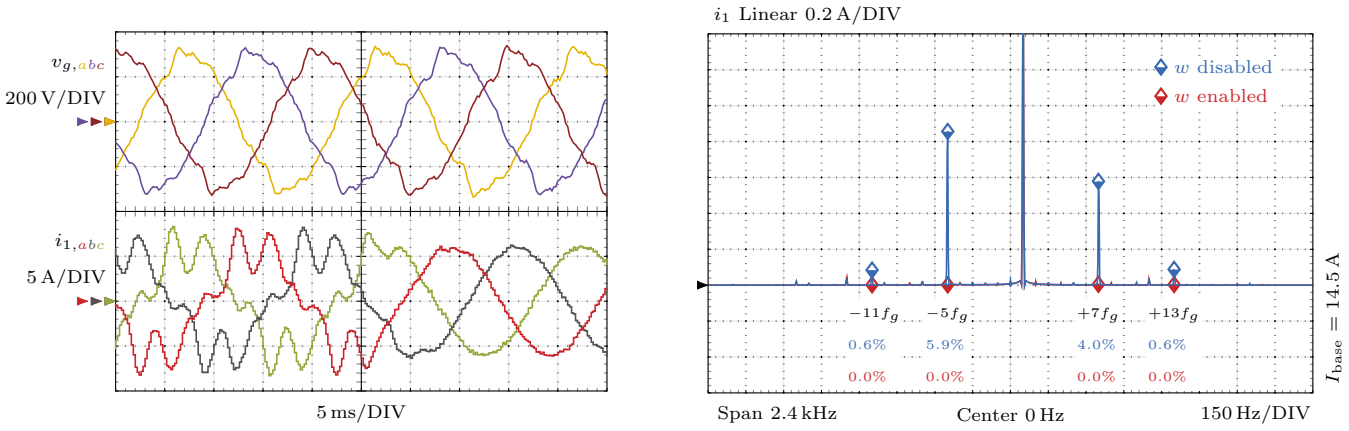

(a) (b)

Fig. 12. Activation of the resonant action of the controller. (a) Time domain. (b) Frequency domain.

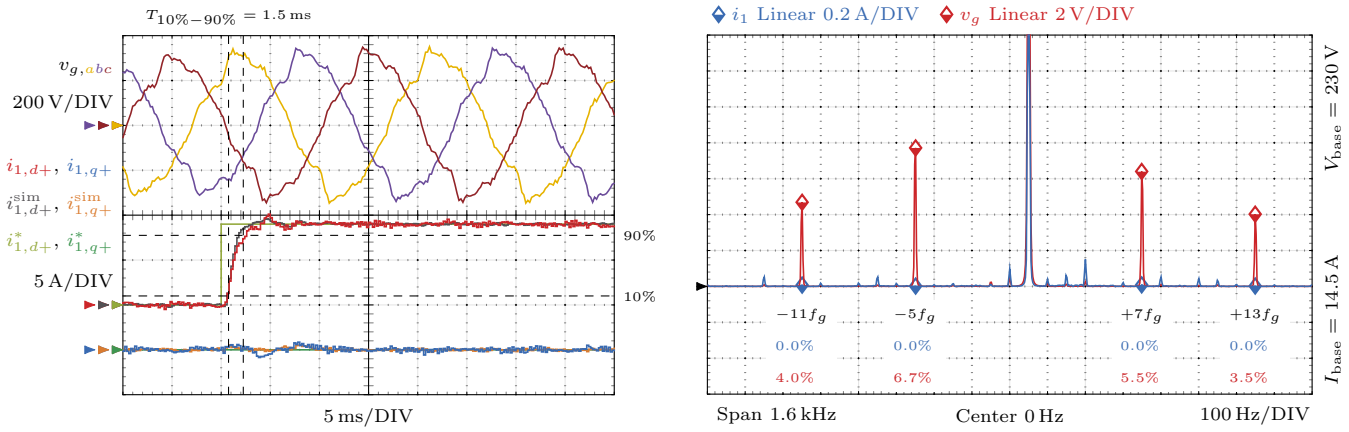

(a) (b)

Fig. 13. Normal operation: the voltage harmonics are balanced. (a) Experimental and simulation waveforms ($i_{1,dq}$ and $i^{sim}_{1,dq}$, respectively) for a reference step $i^{*}_{1,q+}$ in the positive synchronous frame dq+ rotating at the fundamental grid frequency f_g. (b) Experimental spectrum of the grid-side current and the grid-side voltage in the $\alpha\beta$ frame (i_1 and v_g, respectively).

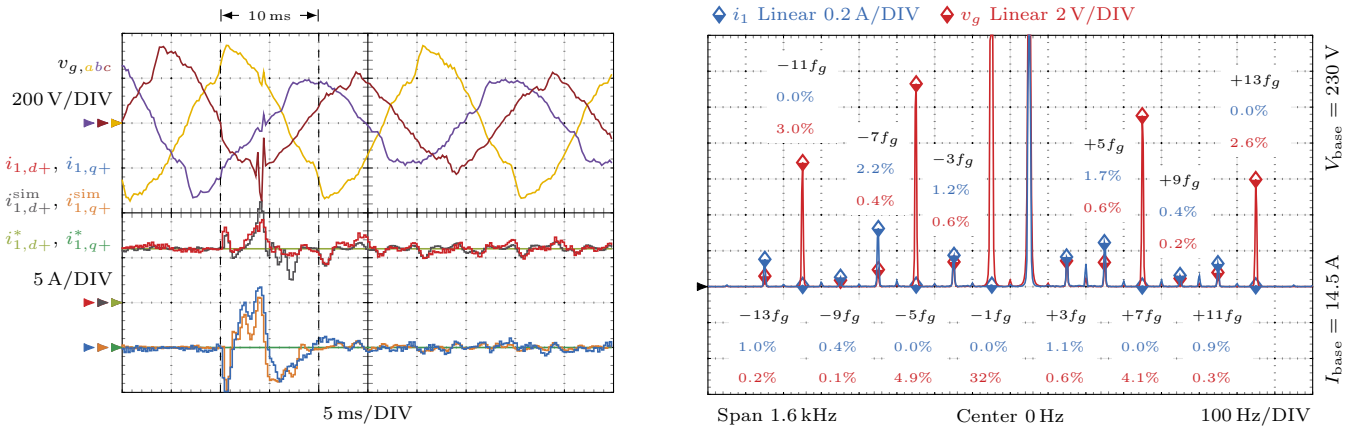

(a) (b)

Fig. 14. Operation during a 40%-depth type-C sag [38]. (a) Experimental and simulation waveforms ($i_{1,dq}$ and $i^{sim}_{1,dq}$, respectively). (b) Experimental spectrum of the grid-side current and the grid-side voltage in the $\alpha\beta$ frame (i_1 and v_g, respectively). Notice that during the sag $v_g(-f_g) \neq 0$ and the voltage harmonics are unbalanced (the spectrum starts being measured 15 ms after the sag event to capture the steady-state regime).

This article has been accepted for publication in a future issue of this journal, but has not been fully edited. Content may change prior to final publication. Citation information: DOI 10.1109/TIA.2018.2829459, IEEE Transactions on Industry Applications

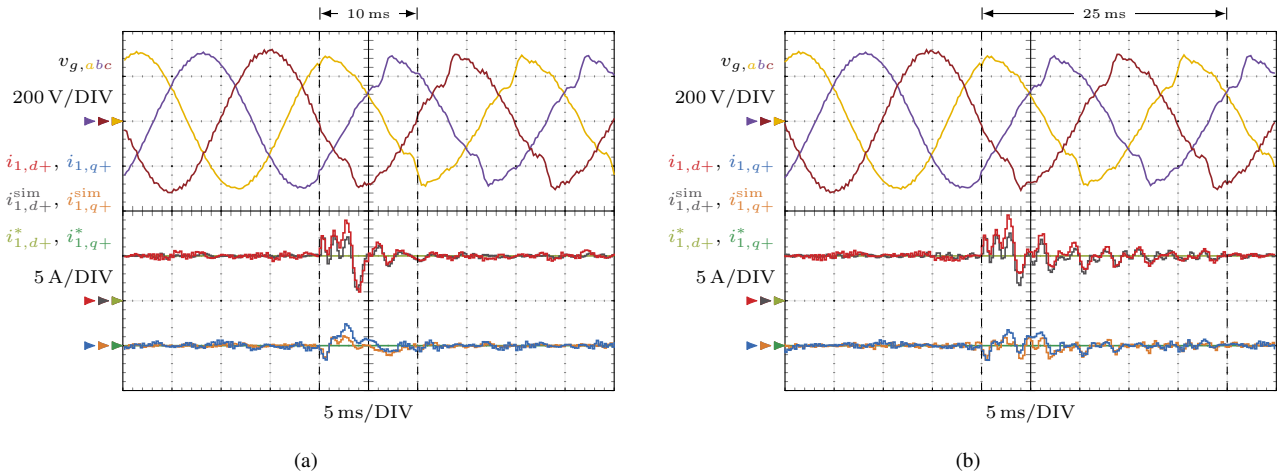

Fig. 15. The grid voltage is changed from a low-distortion situation to the highly distorted voltage defined in Table II. (a) Recommended-bandwidth observer ($\mathbf{Q} = 0.1\%$). (b) Low-bandwidth observer ($\mathbf{Q} = 0.01\%$).

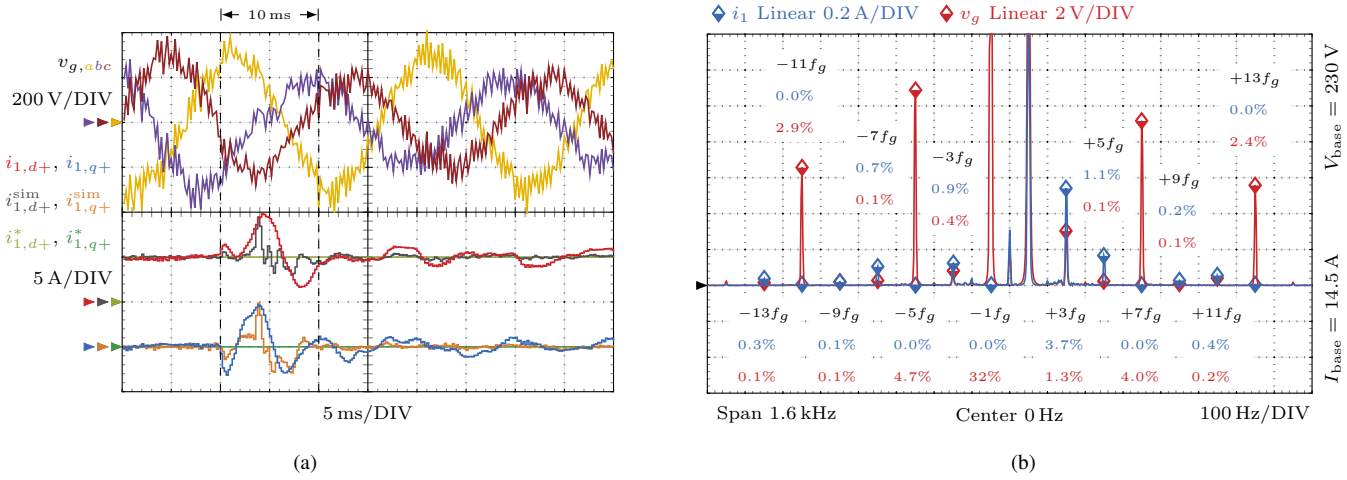

Fig. 16. Operation during a 40%-depth type-C sag [38] with grid impedance of $Z_{\text{g}} = 0.15 + j0.10$ p.u.. (a) Experimental and simulation waveforms ($i_{1,dq}$ and $i^{\text{sim}}_{1,dq}$, respectively). (b) Experimental spectrum of the grid-side current and the grid-side voltage in the $\alpha\beta$ frame (i_1 and v_g, respectively). The spectrum starts being measured 15 ms after the sag event to capture the steady-state regime.

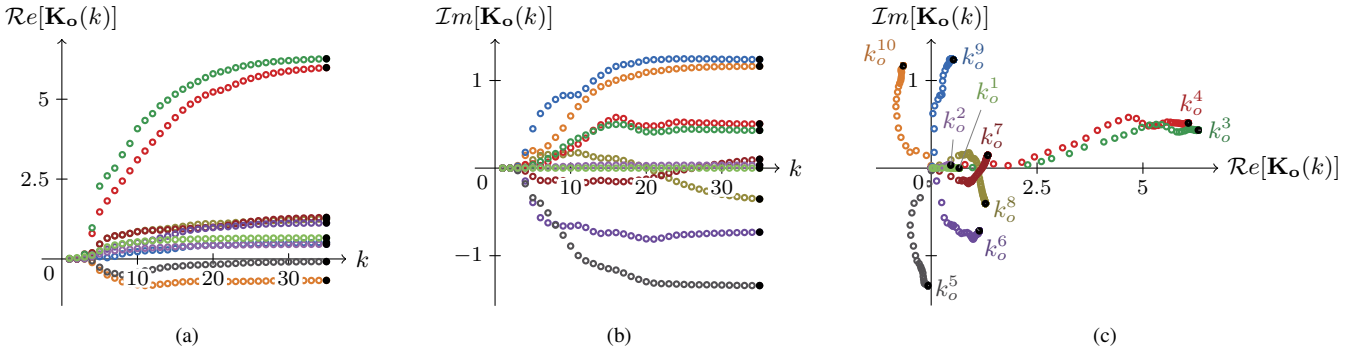

Fig. 17. Result of the first 35 iterations of Algorithm 1 when applied to a system with the parameters shown in Table I. (a) Real component of the elements of the vector $\mathbf{K_o}$. (b) Imaginary component of the elements of the vector $\mathbf{K_o}$. (c) Plot in the complex plane of the elements of the vector $\mathbf{K_o}$.

the model of the plant and the disturbance $\mathbf{F_3}$ and $\mathbf{H_3}$ [cf. (13)]; and a tolerance ϵ, which is used in the stop condition to detect when convergence is achieved. A value of $\epsilon = 10^{-10}$ ensures a good precision in the coefficients.

An analytical solution can be found in [29] and its implementation is available in the Matlab function `kalman`.

Fig. 17 shows the result of the first 35 iterations of Algorithm 1 when applied to a system with the parameters

This article has been accepted for publication in a future issue of this journal, but has not been fully edited. Content may change prior to final publication. Citation information: DOI 10.1109/TIA.2018.2829459, IEEE Transactions on Industry Applications

Algorithm 1 Calculation of the Kalman Gain $\mathbf{K_o}$

Inputs: N, $\mathbf{Q}$, $\mathbf{F_3}$, $\mathbf{H_3}$, ϵ

while $\|\mathbf{K_o}(k+1) - \mathbf{K_o}(k)\|_2 \geq \epsilon$ **do**
  Update values from previous iteration
  $\mathbf{P}(k) \leftarrow \mathbf{P}(k+1)$
  $\mathbf{K_o}(k) \leftarrow \mathbf{K_o}(k+1)$
  Project the error covariance ahead
  $\mathbf{P_p} \leftarrow \mathbf{F_3}\mathbf{P}(k)\mathbf{F_3}^{\mathrm{T}} + \mathbf{Q}$
  Compute the Kalman gain
  $\mathbf{K_o}(k+1) \leftarrow \mathbf{P_p}\mathbf{H_3}^{\mathrm{T}}/(\mathbf{H_3}\mathbf{P_p}\mathbf{H_3}^{\mathrm{T}} + N)$
  Update the error covariance
  $\mathbf{P}(k+1) \leftarrow (\mathbf{I} - \mathbf{K_o}(k+1)\mathbf{H_3})\mathbf{P_p}$
end while

shown in Table I. In this case, the design selected frequencies are the grid-frequency harmonics $+1, -1, -5, +7, -11, +13$; therefore, the obtained gain $\mathbf{K_o}$ is a vector with ten elements: one element for each of the selected frequencies and four elements for the plant model, cf. (5) and (13):

$$\mathbf{K_o} = \begin{bmatrix} k_o^1 & k_o^2 & \cdots & k_o^{10} \end{bmatrix}. \tag{23}$$

It should be noticed that when the selected frequencies are not symmetric with respect to zero hertz, the resultant vector $\mathbf{K_o}$ is complex valued.

Appendix B
Computational Load of the Multi-Frequency Controller

The control equation is (cf. Fig. 3)

$$u(k) = K_{\mathrm{f}} i_1^*(k) + K_{\mathrm{ff}} v_g(k) - \mathbf{K_c}\hat{\mathbf{x}}_{\mathbf{2}} - w. \tag{24}$$

Therefore, the number of operations that the control law requires is 6 complex multiplications and 6 complex additions. Since a complex multiplication requires 6 floating-point operations (flops) and a complex addition is performed in 2 flops, the control law has a constant complexity of 48 flops.

On the other hand, the observer equations are (17) and (18). The state vector of the augmented plant model $\mathbf{x_3}$ increases its size for every new harmonic that is included in the disturbance model. The size of $\mathbf{x_3}$ is $n+4$, e.g., it has three state variables associated to the LCL filter, one to the computational delay, and n to the disturbance model. Thus, the observer requires $2n^2 + 18n + 40$ complex multiplications and $n^2 + 11n + 26$ complex additions. This results in a total of $14n^2 + 130n + 292$ flops for the observer.

Therefore, the total number of flops per second that the current controller executes is $f_s(14n^2 + 130n + 340)$, which is constant for a given number n of controlled harmonics, and increases with n. In the presented implementation ($n = 6$ and $f_s = 5\,\mathrm{kHz}$), a figure of 8.1 mega-flops per second is obtained, which is well below the capability of modern microcontrollers.

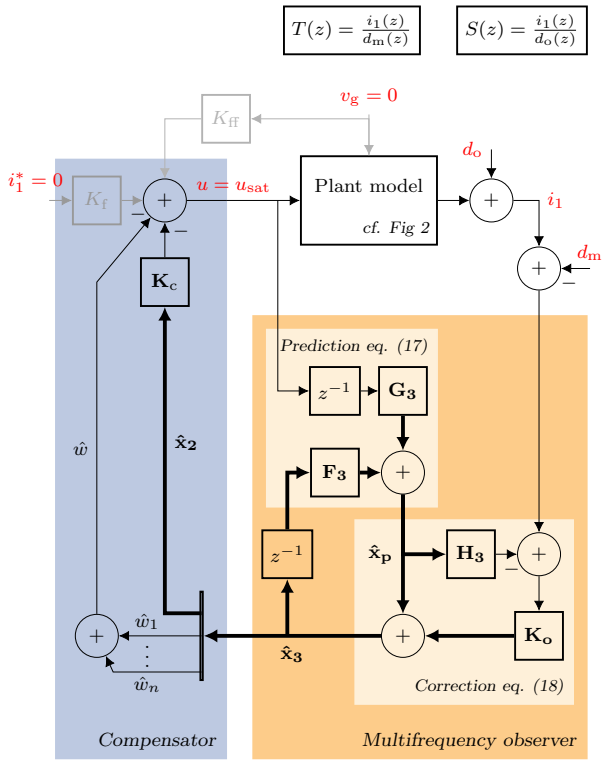

Fig. 18. Block diagram representation of the closed-loop system used to obtain the sensitivity function $S(f)$ and the complementary sensitivity function $T(f)$.

Appendix C
Derivation Process of the Sensitivity and Complementary Sensitivity Functions

The derivation process to obtain the sensitivity function $S(f)$ and the complementary sensitivity function $T(f)$ is detailed below. In order to obtain a transfer function between two variables (an input and an output) the output is calculated as a function of the desired input, assuming the remaining inputs of the system equal to zero.

On the one hand, the sensitivity function $S(f)$ relates a disturbance d_{o} in the grid current with the grid current i_1, see Fig. 18. On the other hand, the complementary sensitivity function $T(f)$ is the ratio of i_1 to a disturbance d_{m} in the measured grid current. Using the block-diagram representation shown in Fig. 18, the state-space model given in (25) on the top of the next page is obtained. Such model relates $i_1(k)$ with $d_{\mathrm{o}}(k)$ and $d_{\mathrm{m}}(k)$.

Therefore, the resultant sensitivity function is

$$S(f) = \frac{i_1}{d_o} = \mathbf{H_{cl}}(e^{j2\pi f T_{\mathrm{s}}}\mathbf{I} - \mathbf{F}_{\mathrm{cl}})^{-1}\mathbf{G_{cl,d_o}} + 1. \tag{26}$$

In addition, the complementary sensitivity function is

$$\begin{aligned} T(f) = \frac{i_1}{d_m} &= \mathbf{H_{cl}}(e^{j2\pi f T_{\mathrm{s}}}\mathbf{I} - \mathbf{F}_{\mathrm{cl}})^{-1}\mathbf{G_{cl,d_m}} \\ &= -S(f) + 1 \end{aligned} \tag{27}$$

which agrees with the fundamental relation in (21).

This article has been accepted for publication in a future issue of this journal, but has not been fully edited. Content may change prior to final publication. Citation information: DOI 10.1109/TIA.2018.2829459, IEEE Transactions on Industry Applications

$$\underbrace{\begin{bmatrix}\mathbf{x}_2(k+1)\\ \mathbf{x}_3(k+1)\\ u_{\mathrm{d}}(k+1)\end{bmatrix}}_{\mathbf{x}_{\mathrm{cl}}(k+1)} = \underbrace{\begin{bmatrix}\mathbf{F_2}-\mathbf{G_2}\mathbf{K_c}\mathbf{K_o}\mathbf{H_2} & -\mathbf{G_2}\mathbf{K_c}(\mathbf{F_3}-\mathbf{K_o}\mathbf{H_3}\mathbf{F_3}) & -\mathbf{G_2}(\mathbf{K_c}\mathbf{G_3}+\mathbf{K_o}\mathbf{H_3}\mathbf{G_3})\\ \mathbf{K_o}\mathbf{H_2} & \mathbf{F_3}-\mathbf{K_o}\mathbf{H_3}\mathbf{F_3} & \mathbf{G_3}-\mathbf{K_o}\mathbf{H_3}\mathbf{G_3}\\ -\mathbf{K_c}\mathbf{K_o}\mathbf{H_2} & -\mathbf{K_c}(\mathbf{F_3}-\mathbf{K_o}\mathbf{H_3}\mathbf{F_3}) & -\mathbf{K_c}(\mathbf{G_3}-\mathbf{K_o}\mathbf{H_3}\mathbf{G_3})\end{bmatrix}}_{\mathbf{F}_{\mathrm{cl}}} \underbrace{\begin{bmatrix}\mathbf{x}_2(k)\\ \mathbf{x}_3(k)\\ u_{\mathrm{d}}(k)\end{bmatrix}}_{\mathbf{x}_{\mathrm{cl}}(k)}$$

$$+\underbrace{\begin{bmatrix}-\mathbf{G_2}\mathbf{K_c}\mathbf{K_o}\\ \mathbf{K_o}\\ -\mathbf{K_c}\mathbf{K_o}\end{bmatrix}}_{\mathbf{G}_{\mathrm{cl},\mathbf{d}_{\mathrm{o}}}} d_{\mathrm{o}}(k) + \underbrace{\begin{bmatrix}\mathbf{G_2}\mathbf{K_c}\mathbf{K_o}\\ -\mathbf{K_o}\\ \mathbf{K_c}\mathbf{K_o}\end{bmatrix}}_{\mathbf{G}_{\mathrm{cl},\mathbf{d}_{\mathrm{m}}}} d_{\mathrm{m}}(k)$$

$$i_1(k) = \underbrace{\begin{bmatrix}\mathbf{H_2} & \mathbf{0}\end{bmatrix}}_{\mathbf{H}_{\mathrm{cl}}} \underbrace{\begin{bmatrix}\mathbf{x}(k)\\ u_{\mathrm{d}}(k)\end{bmatrix}}_{\mathbf{x}_{\mathrm{cl}}(k)} + d_{\mathrm{o}}(k). \tag{25}$$

REFERENCES

[1] B. K. Bose, "Global energy scenario and impact of power electronics in 21st century," *IEEE Trans. Ind. Electron.*, vol. 60, no. 7, pp. 2638–2651, Jul. 2013.

[2] "IEEE recommended practice and requirements for harmonic control in electric power systems," *IEEE Std 519-2014*, pp. 1–29, Jun. 2014.

[3] *Voltage characteristics of electricity supplied by public distribution systems*, CENELEC EN 50160 Std.

[4] P. Channegowda and V. John, "Filter optimization for grid interactive voltage source inverters," *IEEE Trans. Ind. Electron.*, vol. 57, no. 12, pp. 4106–4114, Dec. 2010.

[5] C. A. Busada, S. Gómez Jorge, and J. A. Solsona, "Full-state feedback equivalent controller for active damping in LCL-filtered grid-connected inverters using a reduced number of sensors," *IEEE Trans. Ind. Electron.*, vol. 62, no. 10, pp. 5993–6002, Oct. 2015.

[6] X. Wu, X. Li, X. Yuan, and Y. Geng, "Grid harmonics suppression scheme for LCL-type grid-connected inverters based on output admittance revision," *IEEE Trans. Sust. Energy*, vol. 6, no. 2, pp. 411–421, Mar./Apr. 2015.

[7] T. Abeyasekera, C. M. Johnson, D. J. Atkinson, and M. Armstrong, "Suppression of line voltage related distortion in current controlled grid connected inverters," *IEEE Trans. Power Electron.*, vol. 20, no. 6, pp. 1393–1401, Nov. 2005.

[8] P. Xiao, K. A. Corzine, and G. K. Venayagamoorthy, "Multiple reference frame-based control of three-phase PWM boost rectifiers under unbalanced and distorted input conditions," *IEEE Trans. Power Electron.*, vol. 23, no. 4, pp. 2006–2017, Jul. 2008.

[9] P. L. Chapman and S. D. Sudhoff, "A multiple reference frame synchronous estimator/regulator," *IEEE Trans. Energy Convers.*, vol. 15, no. 2, pp. 197–202, Jun. 2000.

[10] L. R. Limongi, R. Bojoi, G. Griva, and A. Tenconi, "Digital current-control schemes," *IEEE Ind. Electron. Mag.*, vol. 3, no. 1, pp. 20–31, Mar. 2009.

[11] J. Rocabert, A. Luna, F. Blaabjerg, and P. Rodríguez, "Control of power converters in ac microgrids," *IEEE Trans. Power Electron.*, vol. 27, no. 11, pp. 4734–4749, Nov. 2012.

[12] L. Harnefors, A. G. Yepes, A. Vidal, and J. Doval-Gandoy, "Passivity-based stabilization of resonant current controllers with consideration of time delay," *IEEE Trans. Power Electron.*, vol. 29, no. 12, pp. 6260–6263, Dec. 2014.

[13] L. Harnefors, A. G. Yepes, A. Vidal, and J. Doval-Gandoy, "Passivity-based controller design of grid-connected VSCs for prevention of electrical resonance instability," *IEEE Trans. Ind. Electron.*, vol. 62, no. 2, pp. 702–710, Jan./Feb. 2015.

[14] F. Briz, P. García, M. W. Degner, D. Díaz-Reigosa, and J. M. Guerrero, "Dynamic behavior of current controllers for selective harmonic compensation in three-phase active power filters," *IEEE Trans. Ind. Appl.*, vol. 49, no. 3, pp. 1411–1420, May/Jun. 2013.

[15] B. Li, W. Yao, L. Hang, and L. M. Tolbert, "Robust proportional resonant regulator for grid-connected voltage source inverter (VSI) using direct pole placement design method," *IET Power Electron.*, vol. 5, no. 8, pp. 1367–1373, Sep. 2012.

[16] A. Vidal, F. D. Freijedo, A. G. Yepes, J. Malvar, O. López, and J. Doval-Gandoy, "Transient response evaluation of stationary-frame resonant current controllers for grid-connected applications," *IET Power Electron.*, vol. 7, no. 7, pp. 1714–1724, Jul. 2014.

[17] M. Liserre, R. Teodorescu, and F. Blaabjerg, "Stability of photovoltaic and wind turbine grid-connected inverters for a large set of grid impedance values," *IEEE Trans. Power Electron.*, vol. 21, no. 1, pp. 263–272, Jan. 2006.

[18] H. Eldeeb, A. Massoud, A. S. Abdel-Khalik, and S. Ahmed, "A sensorless kalman filter-based active damping technique for grid-tied vsi with LCL filter," *Intern. Journal of Elec. Power and Energy Systems*, vol. 93, no. Supplement C, pp. 146 – 155, 2017. [Online]. Available: http://www.sciencedirect.com/science/article/pii/S0142061517304520

[19] Z. Xin, P. Mattavelli, W. Yao, Y. Yang, F. Blaabjerg, and P. C. Loh, "Mitigation of grid current distortion for LCL-filtered voltage source inverter with inverter current feedback control," *IEEE Transactions on Power Electronics*, To be published.

[20] B. Li, M. Zhang, L. Huang, L. Hang, and L. M. Tolbert, "A new optimized pole placement strategy of grid-connected inverter with LCL-filter based on state variable feedback and state observer," in *App. Power Electron. Conf. and Exp. (APEC)*, Mar. 2013, pp. 2900–2906.

[21] J. Kukkola, M. Hinkkanen, and K. Zenger, "Observer-based state-space current controller for a grid converter equipped with an LCL filter: Analytical method for direct discrete-time design," *IEEE Trans. Ind. Appl.*, vol. 51, no. 5, pp. 4079–4090, Sep./Oct. 2015.

[22] D. Pérez-Estévez, J. Doval-Gandoy, A. G. Yepes, and O. López, "Positive- and negative-sequence current controller with direct discrete-time pole placement for grid-tied converters with LCL filter," *IEEE Trans. Power Electron.*, vol. 32, no. 9, pp. 7207 – 7221, 2017.

[23] X. Wang, F. Blaabjerg, and P. C. Loh, "Grid-current-feedback active damping for LCL resonance in grid-connected voltage-source converters," *IEEE Trans. Power Electron.*, vol. 31, no. 1, pp. 213–223, Jan. 2016.

[24] J. Wang, J. D. Yan, L. Jiang, and J. Zou, "Delay-dependent stability of single-loop controlled grid-connected inverters with LCL filters," *IEEE Trans. Power Electron.*, vol. 31, no. 1, pp. 743–757, Jan. 2016.

[25] J. Xu, S. Xie, and T. Tang, "Active damping-based control for grid-connected LCL-filtered inverter with injected grid current feedback only," *IEEE Trans. Ind. Electron.*, vol. 61, no. 9, pp. 4746–4758, Sep. 2014.

[26] S. G. Parker, B. P. McGrath, and D. G. Holmes, "Regions of active damping control for LCL filters," *IEEE Trans. Ind. Appl.*, vol. 50, no. 1, pp. 424–432, Jan./Feb. 2014.

[27] D. Pérez-Estévez, J. Doval-Gandoy, A. G. Yepes, O. López, and F. Baneira, "Multi-frequency current controller for grid-tied converters," in *IEEE Energy Conv. Congress and Exp.*, Oct. 2017, pp. 3897–3904.

[28] A. Vidal, A. G. Yepes, F. D. Freijedo, J. Malvar, O. López, and J. Doval-Gandoy, "A technique to estimate the equivalent loss resistance of grid-tied converters for current control analysis and design," *IEEE Trans. Power Electron.*, vol. 30, no. 3, pp. 1747–1761, Mar. 2015.

[29] G. F. Franklin, J. D. Powell, and M. L. Workman, *Digital Control of Dynamic Systems*, 3rd ed. Addison Wesley Longman, Inc, 1998, pp. 202–203, 110, 322–336, 308–309, 400–403, 289–301, 286.

[30] G. C. Goodwin, S. F. Graebe, and M. E. Salgado, *Control System Design*, 1st ed. Prentice Hall, 2001, p. 355.

[31] D. Pérez-Estévez, J. Doval-Gandoy, A. G. Yepes, O. López, and F. Baneira, "Enhanced resonant current controller for grid-connected con-

verters with LCL filter," *IEEE Trans. Power Electron.*, Accepted for publication.

[32] A. G. Yepes, J. Malvar, A. Vidal, O. López, and J. Doval-Gandoy, "Current harmonics compensation based on multiresonant control in synchronous frames for symmetrical *n*-phase machines," *IEEE Trans. Ind. Electron.*, vol. 62, no. 5, pp. 2708–2720, May 2015.

[33] C. Mohtadi, "Bode's integral theorem for discrete-time systems," *IEE Proceedings D - Control Theory and Applications*, vol. 137, no. 2, pp. 57–66, Mar. 1990.

[34] A. Papoulis and S. U. Pillai, *Probability, Random Variables and Stochastic Processes*, McGraw-Hill, Ed. McGraw-Hill, 2002.

[35] M. Lu, X. Wang, F. Blaabjerg, S. M. Muyeen, A. Al-Durra, and S. Leng, "Grid-voltage-feedforward active damping for grid-connected inverter with LCL filter," in *App. Power Electron. Conf. and Exp. (APEC)*, Mar. 2016, pp. 1941–1946.

[36] M. Liserre, F. Blaabjerg, and S. Hansen, "Design and control of an LCL-filter-based three-phase active rectifier," *IEEE Trans. Ind. Appl.*, vol. 41, no. 5, pp. 1281–1291, Sep./Oct. 2005.

[37] F. D. Freijedo, J. Doval-Gandoy, O. López, and E. Acha, "Tuning of phase-locked loops for power converters under distorted utility conditions," *IEEE Trans. Ind. Appl.*, vol. 45, no. 6, pp. 2039–2047, Nov./Dec. 2009.

[38] M. H. Bollen, *Understanding Power Quality Problems: Voltage Sags and Interruptions*, 1st ed. Wiley, 1999, p. 194.

Diego Pérez-Estévez (S'15) received the M.Sc. degree in telecommunications engineering, in 2014, from the University of Vigo, Vigo, Spain, where he is currently working toward the Ph.D. degree in the Applied Power Electronics Technology Research Group.

Since 2014, he has been with the Applied Power Electronics Technology Research Group. His research interests include control of grid-connected converters and distributed power generation systems.

Jesús Doval-Gandoy (M'99) received the M.S. and Ph.D. degrees in electrical engineering from the Polytechnic University of Madrid, Madrid, Spain, and from the University of Vigo, Vigo, Spain, in 1991 and 1999 respectively.

He is a Professor and the head of the Applied Power Electronics Technology Research Group (APET), University of Vigo. His research interests are in the areas of ac power conversion.

Alejandro G. Yepes (S'10-M'12) received the M.Sc. and Ph.D. degrees in electrical engineering from the University of Vigo, Vigo, Spain in 2009 and 2011, respectively.

Since 2008, he has been with the Applied Power Electronics Technology Research Group, University of Vigo. His research interests are in the areas of ac power conversion, with special focus, currently, on multiphase drives and digital control of power electronics converters.

Oscar López (M'05-SM'16) received the M.Sc. and Ph.D. degrees in electrical engineering from the University of Vigo, Vigo, Spain, in 2001 and 2009, respectively.

Since 2004, he has been an Assistant Professor at the University of Vigo. He is a member of the Applied Power Electronics Technology Research Group, University of Vigo. His research interests include the areas of ac power switching converters technology.

Fernando Baneira (S'15) received the M.Sc. degree in electrical engineering from the University of Vigo, Vigo, Spain, in 2013, where he has been working toward the Ph.D. degree in the Applied Power Electronics Technology Research Group since 2014.

His research interests include power electronics, multiphase systems, and ac drives.